Geophysical Journal International

Geophys. J. Int. (2012) **188,** 447–472 doi: 10.1111/j.1365-246X.2011.05277.x

Chemical and magnetic properties of rapidly cooled metastable ferri-ilmenite solid solutions: implications for magnetic self-reversal and exchange bias—II. Chemical changes during quench and annealing

Peter Robinson,[1,2] Richard J. Harrison,[3] Nobuyoshi Miyajima,[2] Suzanne A. McEnroe[1,2] and Karl Fabian[1]

[1] *Geological Survey of Norway,* N-7491 *Trondheim, Norway. E-mail: peter.robinson@ngu.no*
[2] *Bayerisches Geoinstut, Universität Bayreuth,* D95440 *Bayreuth, Germany*
[3] *Department of Earth Sciences, University of Cambridge, Cambridge* CB2 3EQ*, UK*

Accepted 2011 October 19. Received 2011 October 14; in original form 2011 August 3

SUMMARY

Chemical and microstructural evolution during quench and short-term annealing of a sample $X\mathrm{FeTiO_3} = 0.61$ is explored in the light of observations in Paper I. Ordering proceeds by (1) random appearance of ordered and anti-ordered domains within a disordered host, (2) coarsening of ordered and anti-ordered domains until they impinge along antiphase domain boundaries, (3) growth of regions where one ordered or anti-ordered phase becomes dominant over the other, with progressive reduction in surface area of antiphase domain boundaries and (4) dynamic development where antiphase boundaries migrate during annealing, leading to Fe enrichment of shrinking domains and Fe depletion of growing domains. These conclusions are supported by 2-D Monte Carlo simulations illustrating that Ti–Ti avoidance is a powerful driving force for Fe enrichment along antiphase boundaries, and by bond-valence calculations demonstrating that local charge balance is improved when antiphase domain boundaries contain a combination of Fe-rich contact layers and disordered boundary layers along (001). Chemical phase separation during quenching is driven by the disorder/order transition at temperatures above the tricritical point and by spinodal decomposition at temperatures below the tricritical point. The former explains microtextures and chemical features in samples quenched from high temperature; the latter produces textural and chemical evolution during subsequent annealing. All these features provide the atomic basis for self-reversed thermoremanent magnetization and room-temperature magnetic exchange bias as will be described in Paper III.

Key words: Magnetic mineralogy and petrology; Rock and mineral magnetism; Microstructures.

1 INTRODUCTION

Paper I of this series (Fabian *et al*. 2011) gave a detailed magnetic, crystallographic and chemical description of a quenched synthetic sample of the solid solution $X\mathrm{FeTiO_3} + (1–X)\mathrm{Fe_2O_3}$ with composition $X = 0.61$. This sample had experienced partial Fe–Ti ordering and substantial chemical phase separation during the quench, leading to the presence of two phases interacting magnetically across their interfaces. Transmission electron microscopy energy dispersive X-ray (TEM–EDX) analyses revealed the presence of an Fe-poor ferrimagnetic phase with composition $X = 0.61–0.64$ together with a dominant Fe-rich antiferromagnetic phase with composition $X = 0.56–0.61$. After annealing for a few minutes below the Fe–Ti ordering temperature (T), the sample attained the key properties of self-reversed thermoremanent magnetization and modest room-T magnetic exchange bias. Such properties are consistent with the presence of a slightly Fe-enriched weakly ordered ferrimagnetic phase with a higher Curie T and high coercivity, and a slightly Fe-depleted phase with a lower Curie T and lower coercivity (Uyeda 1958; Ishikawa & Syono 1963; Nord & Lawson 1989; Prevot *et al*. 2001; Lagroix *et al*. 2004; Harrison *et al*. 2005). Here we explore the detailed nature of the interfaces between disordered, ordered and anti-ordered phases and their evolution during quenching and annealing, and also the probable thermodynamic basis for chemical phase separation. These results then lead in Paper III to detailed examination of the magnetic interactions that occur across

the phase interfaces and the processes taking place as a function of T and applied field when remanence is acquired during further cooling.

2 PREVIOUS TEM STUDIES OF EXPERIMENTAL SAMPLES

When Fe–Ti ordering occurs during cooling in a rhombohedral Fe–Ti oxide, the initial placement of alternate Ti layers occurs at random through the structure. Ordered domains with opposed placement but identical structure, here termed A and B domains, grow outwards until they impinge, producing narrow regions where the phases are chemically out-of-phase and/or locally disordered, described as antiphase domain or twin-domain boundaries. Such boundaries are energetically unfavourable and tend towards elimination with progressive cooling. These boundaries are observed in TEM dark field images through the (003) reflection where ordered phases appear light, and disordered phases and boundaries appear dark (Fig. 1).

The TEM studies by Nord & Lawson (1989, 1992) and Nord (1994), which describe the results of carefully controlled quenching and annealing experiments on compositions $X = 0.60$, 0.70 and 0.80, represent a landmark in this field. Nord & Lawson (1989) observed that samples, annealed below the critical T for Fe–Ti ordering lacked antiphase boundaries whereas samples quenched from above the critical T developed antiphase boundaries on a length scale that varied greatly as a function of composition and quench T. Their sample with composition $X = 0.60$ quenched from 1173 K (i.e. just above the ordering T of 1100 K) most closely resembles our sample with composition $X = 0.61$ (Fabian *et al*. 2011) quenched from 1328 K (Fig. 1). Both samples contain elongate ordered regions less than 10 nm thick in a disordered matrix. The elongation direction is parallel to (001), which provides the best fit of lattice parameters between ordered and disordered phases. Other samples in simple quench experiments had the following compositions, quench T's, corresponding ordering T's and average ordered domain widths, respectively: $X = 0.65$, 1573 K, 1190 K, 30 nm; $X = 0.70$, 1573 K, 1275 K, 0.70 nm and $X = 0.80$, 1573 K, 1450 K, $>$100 nm. This shows that more ilmenite-rich compositions order at higher T's and can achieve coarser intergrowths during quench.

A second group of Nord and Lawson cooling experiments was done on composition $X = 0.70$, held for 48 hr at 1573 K then cooled and held for 10 hr at 1573, 1473, 1373 and 1323 K, all above the 1275 K ordering T, before quench. Typical domain thicknesses are 60, 50, 30 and 20 nm, respectively. Thus, the higher the quench T is above the ordering T, the fewer the boundaries and the coarser the intergrowth. Conversely, when the quench is close above the ordering T, boundaries are more abundant and the intergrowth finer. Apparently the time taken during high T in the quench determines coarseness achieved by the intergrowth. Samples quenched close to the ordering T have a very short time at T for coarsening.

A third group of Nord and Lawson cooling experiments was done on composition $X = 0.70$. Samples were quenched after annealing at 1323 K yielding fine intergrowths (see above), then annealed for different times of 0.1, 1, 10 and 100 hr at 1073 K below the transition T of 1275 K before a second quench. A high density of domain boundaries was only preserved with annealing times well less than 1 hr, illustrating the key role of annealing below the ordering T after quench in increasing the size of ordered domains. Progressive elimination of domain walls takes place, necessarily requiring their rapid movement and amalgamation throughout the crystal. A key part of the coarsening process, which can be frozen in progress, is that a part of the crystal becomes dominated by A-ordered domains with small B-ordered domains whereas other parts become dominated by B-ordered domains with small A-ordered domains. This last aspect of the annealing turns out to be the key to the special magnetic properties in such samples.

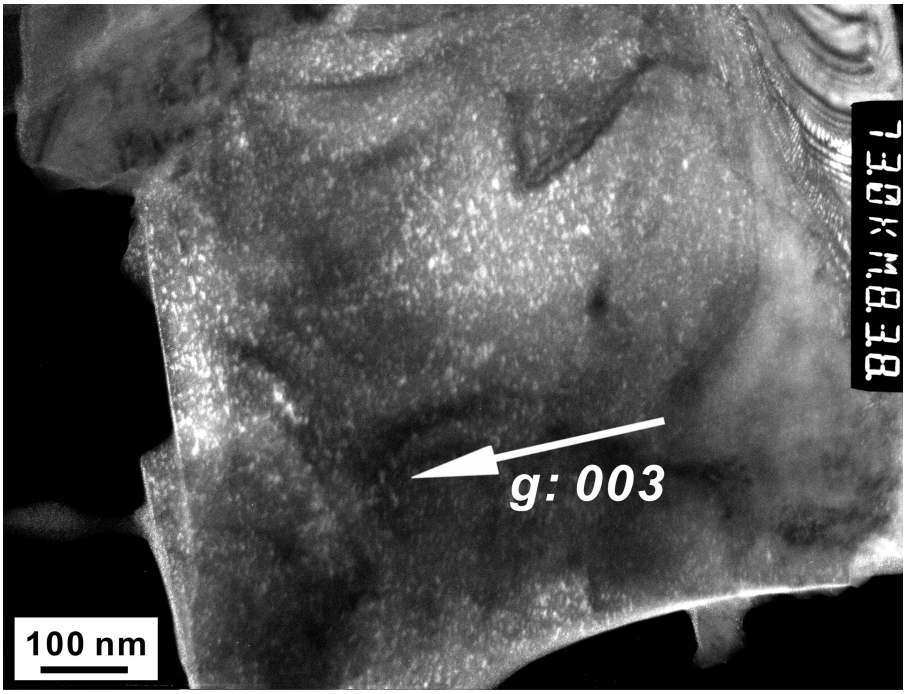

Figure 1. Dark-field TEM image of Ilm 60 (1055 °C) taken through the ilmenite-like ordered reflection $g = 003$, where only the ordered regions are illuminated, representing a minority of the sample. Note that the ordered regions are slightly elongated parallel to (001). 150 TEM–EDX analyses (Fabian *et al*. 2011) were collected in three traverses close to the feather edge at left centre.

3 OBSERVATION OF Fe–Ti ORDER AT T

The powder neutron diffraction experiments at T on compositions $X = 0.60$ and 0.65 of Harrison & Redfern (2001) provide strong evidence concerning the behaviour of Fe–Ti ordering. They determined average atomic occupancy of alternating Ti- and Fe-rich (A and B) ordered layers, and thus the order parameter $Q = (X\text{TiA} - X\text{TiB})/(X\text{TiA} + X\text{TiB})$, ranging from 0 (completely disordered) to 1.0 (completely ordered). Before heating and cooling runs, samples were quenched from 1300 °C producing intergrowths of ordered and disordered phases, probably similar to those in Fig. 1. In the run for $X = 0.60$ no diffraction was done below 200 °C to avoid magnetic peaks that confuse patterns from atomic diffraction. Results at 203, 298 and 399 °C gave $Q = 0.400$, 0.387 and 0.447, considered to be average values over ordered and disordered regions in the quenched sample. Actual degree of order in ordered regions could be estimated only if there is an independent estimate of the volume fraction of the ordered phase.

During heating through 498, 506, 549 and 598 °C, there was 'relaxation', probably involving growth of ordered regions at the expense of disordered regions, yielding average Q's 0.577, 0.650, 0.677 and 0.703, respectively. The Q of approximately 0.70, after this relaxation, could be the same Q achieved in the ordered part of the sample during quench, but there is little basis for this assumption. At higher T's 647, 697, 721, 745, 793 and 818 °C, Q's fell sequentially 0.693, 0.640, 0.590, 0.463, 0.360 and 0, representing equilibrium degrees of order. The sample annealed for 39 months at 685–690 °C (Burton *et al*. 2008) was at a T close to the 697 °C neutron sample with $Q = 0.640$. Measurements at 844, 921 and 999 °C all gave $Q = 0$. During slow cooling through 795, 594, 392 and 203 °C, Q's rose sequentially 0.340, 0.783, 0.883 and 0.907, showing that high order results from slow cooling.

4 ENERGETICS OF Fe–Ti ORDERING

The Gibbs free energy (G) of the Fe–Ti system depends both on the cation order parameter (Q) and the chemical composition (X). The variation of G with X is discussed in Section 9.2 and Appendix D. The variation of G with Q for fixed X is illustrated schematically in Fig. 2 at a T below the disorder-order transition, where $Q = 0$ for complete disorder, +1.0 for perfectly A-ordered, and –1.0 for perfectly B-ordered (anti-ordered) arrangements. This shows an equally low G for A- or B-ordered phases, with Q approximately equal to +0.90 and –0.90, compared to the disordered phase, and also shows a spinodal region between $Q = +0.43$ and –0.43, where sinusoidal fluctuations in Q can develop spontaneously without requirement for nucleation, creating regions of partial A- and B-order, separated by disordered boundary regions. In Section 9, we explore how chemical spinodal phenomena must also be involved in phase evolution during quench and annealing. In the following section we explore the possible cation distributions that might arise when A-ordered, B-ordered and disordered regions within the crystal impinge.

5 2-D MONTE CARLO SIMULATION OF PHASE SEPARATION

Three key assertions underpin the chemical models presented in this paper: (1) that the boundaries between ordered and anti-ordered domains are Fe enriched; (2) that the transition from short-range order to long-range order is achieved by the growth of large domains at the expense of small domains (Ostwald ripening) and (3) that small domains become Fe enriched relative to large domains during ripening. Justification for these assertions has been provided by Harrison *et al*. (2005) and Harrison (2006) for the specific case of the ilmenite–haematite solid solution. Here we demonstrate, using a simple 2-D simulation of an A–B alloy, that the assumptions underpinning this study are a natural consequence of the drive to eliminate energetically unfavourable nearest-neighbour atom pairs, and therefore that they are likely to be a general feature of any quenched solid solution that shows a tendency to order.

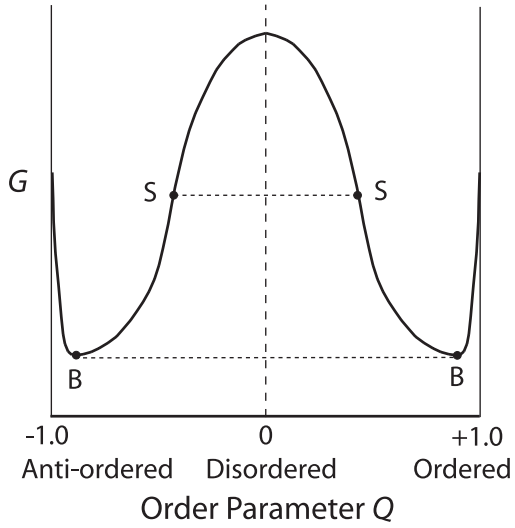

Figure 2. Schematic graph of Gibbs free energy (G) versus the order parameter Q for composition $X = 0.60$, at some T below the Fe–Ti order disorder transition, where $Q = 0$ for complete disorder, +1.0 for A-ordered and –1.0 for B-ordered (anti-ordered) arrangements. The curve shows two minima (binodes) for the two ordered arrangements and a maximum for the disordered arrangement. Inflection points (spinodes) at the boundaries between negative and positive curvature mark the boundaries of the region for spinodal decomposition, where waves of opposing partially ordered and partially anti-ordered phases can develop spontaneously without requirement for nucleation.

Consider a 2-D square lattice (Fig. 3a), with alternating squares labelled α and β for reference. Onto each site we can place either an A or a B atom. The proportions of A and B atoms are defined by the composition parameter x_A

$$x_A = N_A/(N_A + N_B), \tag{1}$$

where N_A and N_B are the numbers of A and B atoms, respectively. For display purposes, atoms are colour-coded according whether they occupy an α or a β site. An A atom sitting on an α site is blue, an A atom sitting on a β site is yellow and B atoms are black, irrespective of which site they are on. The energy of the system can be expressed in terms of the number of energetically unfavourable A–A nearest-neighbour pairs, N_{AA} (see Appendix A)

$$E = E_0 - J\,N_{AA}, \tag{2}$$

where E_0 and J are constants. For positive values of J, the energy is reduced by maximizing N_{AA}. This is achieved by phase separation into regions of pure A and pure B (exsolution). For negative values of J, the energy is reduced by minimizing N_{AA}. This is achieved by ordering, so that each A atom prefers to be surrounded by B nearest neighbours. The ordered phase is visible in the simulations as either blue–black (A on α, B on β) or yellow–black (A on β, B on α) chessboard patterns (Figs 3b–d).

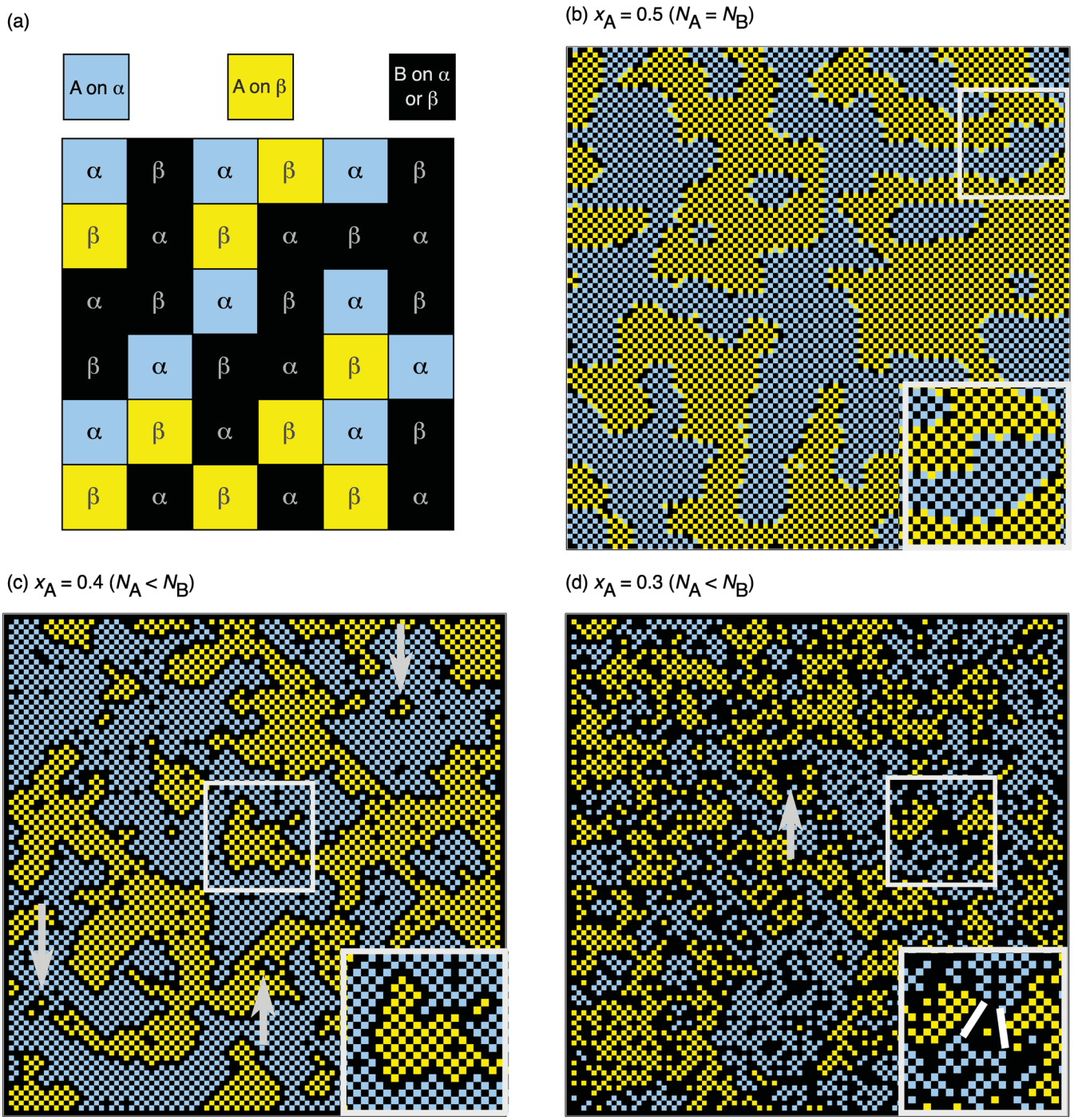

Figure 3. 2-D Monte Carlo simulations showing the effects of ordering of originally random distributions of Ti and Fe atoms for different compositions, where ordering is based on avoidance of thermodynamically unfavourable occurrence of Ti in adjacent sites (see Appendix A). (a) Checkerboard array of α and β sites, where blue colour denotes A ions (Ti) in α sites and yellow colour denotes A ions (Ti) in β sites. Black denotes B ions (Fe) in either α or β sites. (b) Simulation after 10^6 iterations for composition $N_A = N_B$ or $X_A = 0.5$ corresponding Ti/(Ti + Fe) = 0.5 or $X\mathrm{FeTiO_3} = 1.0$. (c) Simulation for composition $N_A < N_B$ or $X_A = 0.4$ corresponding to Ti/(Ti + Fe) = 0.4 or $X\mathrm{FeTiO_3} = 0.80$. (d) Simulation for composition $N_A < N_B$ or $X_A = 0.3$ corresponding to Ti/(Ti + Fe) = 0.6 or $X\mathrm{FeTiO_3} = 0.60$. The figure parts (c) and (d) illustrate the power of order to create accumulation of B (Fe) ions along the borders of alternately ordered regions.

Monte Carlo simulations (see Appendix A) were used to explore the evolution of the system for the case of negative J. To simulate the effects of rapid cooling, the system was initialized with a random distribution of A and B atoms in proportions determined by x_A (eq. 1) and then annealed at a low T. The system is driven to eliminate A–A pairs, resulting in the rapid formation of ordered (blue–black) and anti-ordered (yellow–black) domains. Results for $x_A = 0.5$ (i.e. equal numbers of A and B atoms) are shown in Fig. 3(b). Perfectly ordered and anti-ordered domains are clearly visible, with complete elimination of A–A nearest-neighbour pairs within the domain interiors. The antiphase boundaries, however, are disordered and contain numerous A–A nearest-neighbour pairs (see inset to Fig. 3b).

Although these boundary pairs represent a significant energy penalty for the system, eliminating them would require introducing a higher number of pairs in the domain interior (because the A:B ratio is 1:1, any further incorporation of A into the domain interior would necessarily introduce A–A nearest neighbours). Results for $x_A = 0.4$ are shown in Fig. 3(c). Because there are now more B atoms than A atoms in the system, A–A nearest-neighbour pairs can be fully eliminated by migrating excess B atoms to the antiphase boundaries. A region at least two B atoms thick decorates all the antiphase boundaries (see inset to Fig. 3c). Enrichment of B atoms at the boundaries creates a shift in the composition of the domain interior towards $x_A = 0.5$, with the magnitude of the shift depending on the surface area to volume ratio of the domains. Small domains of anti-order, marked with arrows in Fig. 3(c), become significantly enriched in B before their elimination during prolonged annealing. Results for $x_A = 0.3$ are shown in Fig. 3(d). Compositional heterogeneities are significantly enhanced as each ordered domain is now further from a 1:1 ratio. Thicker B-enriched boundaries are more common and the B enrichment of small domains of anti-order is more obvious. Chance impingement of B-poor and B-rich ordered domains leads to the presence of 'synphase' boundaries, as discussed in Section 6 (see inset to Fig. 3d: synphase boundaries are shown as a white lines).

These simulations lead us to the general principle that enrichment of antiphase boundaries by the majority atom occurs naturally when the system is driven to order by the elimination of nearest-neighbour pairs of the minority atom. Except for pure $FeTiO_3$, which has equal numbers of Fe and Ti atoms, the ilmenite–haematite solid solution contains an excess of Fe atoms relative to Ti atoms. The overwhelming driving force for ordering is the elimination of Ti–Ti pairs across the shared face of adjacent octahedra. Hence Fe enrichment of antiphase boundaries is a natural consequence of ordering, and will be enhanced further by the development contact layers as discussed in Section 6. It is also expected that as small islands of anti-order—fighting against rising tide of long-range order—start to shrink, they inevitably become Fe enriched with respect to the surrounding sea of ordered domains.

6 DETAILED STRUCTURE OF PHASE INTERFACES

In the case of major phase separation between haematite and ilmenite, it has been proved that 'contact layers', one cation layer thick, develop between haematite and ilmenite (Robinson *et al*. 2002, 2004, 2006). These are single atomic layers, with average compositions between haematite Fe^{3+} layers and ilmenite Fe^{2+} layers. They form at phase interfaces to reduce ionic charge imbalance. Their characteristics have been demonstrated by Monte Carlo simulations (Harrison & Becker 2001; Robinson *et al*. 2002, 2004), by bond-valence calculations (Robinson *et al*. 2006), by density functional theory (Pentcheva & Nabi 2008) and most recently by Mössbauer spectroscopy (McCammon *et al*. 2009). Their critical role at phase interfaces between haematite and ilmenite has recently been demonstrated in studies of magnetic exchange bias in naturally exsolved samples at very low T (McEnroe *et al*. 2007a, b; Fabian *et al*. 2008), by Monte Carlo modelling of exchange bias (Harrison *et al*. 2007) and by neutron diffraction of a natural sample showing extreme exchange bias (Harrison *et al*. 2010). The Fe^{2+}–Fe^{3+} contact layers on lamellar interfaces are magnetically significant because they produce an uncompensated spin, as described in the above papers, but they are also significant in considering chemical constitution.

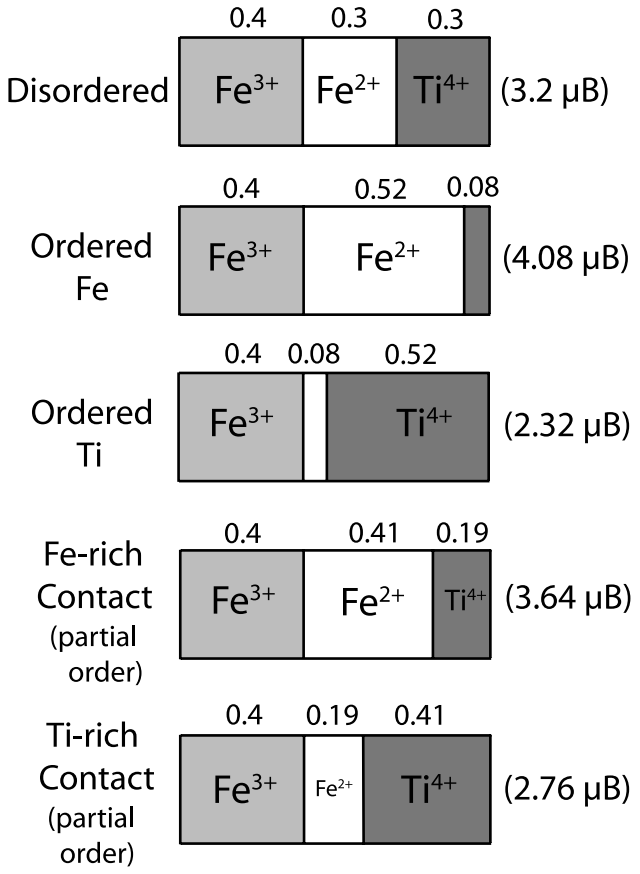

Figure 4. Schematic blocks, each one cation layer thick parallel to (001), used to illustrate the nature of progressive Fe–Ti ordering and phase interfaces in composition $X = 0.60$. In this example, a Q value of 0.73 is used for the ordered phase in calculating interface charge imbalance, although the actual Q value is likely to vary during the ordering process. Numbers in parentheses indicate theoretical magnetic moments in Bohr magnetons (μ_B) at 0 K for each layer composition. From this, one can derive the theoretical ferrimagnetic moment per formula unit of the ordered phase, $4.08\ \mu_B - 2.32\ \mu_B = 1.76\ \mu_B$ (compare with magnetite $\sim 4\ \mu_B$).

The kinds of single atomic layers parallel to (001) that might occur in samples containing both disordered and ordered phases of composition $X = 0.60$ are illustrated as a series of blocks in Fig. 4. Available crystallographic data indicates that, to a first approximation, Fe–Ti ordering involves only Fe^{2+} and Ti^{4+}, not Fe^{3+}. Thus, all the different representational blocks illustrate a constant Fe^{3+} fraction of 0.4 appropriate for the $X = 0.60$ composition. In the top disordered block Fe^{2+} and Ti^{4+} are in equal amounts. For ordered configurations we have arbitrarily assumed a value of $Q = 0.733$, roughly equivalent to the 'relaxed' value observed in the neutron diffraction measurements of Harrison & Redfern (2001) and Harrison *et al.* (2000). Thus, the Fe layers contain the fraction 0.52 Fe^{2+} ions and 0.08 Ti^{4+}, and the Ti layers contain 0.08 Fe^{2+} and 0.52 Ti^{4+}.

The chemical contact layers should also develop along the (001) interfaces between disordered and ordered phases, both with the identical composition $X = 0.60$. Relationships presented in Appendix B, Table B1 show that charge imbalance can be just as problematic along such interfaces, as along interfaces of phases of vastly different compositions. For haematite–ilmenite interfaces, it is inherent that a Ti-rich layer is not comfortable adjacent to an Fe^{3+}-rich layer, and would prefer to be separated from it by a layer with

a larger Fe^{2+} component. Thus contact layers develop. If ordered A domains were directly juxtaposed against ordered B domains along (001), then the interfaces would necessarily have either two juxtaposed ordered Ti layers or two juxtaposed ordered Fe^{2+} layers and this would lead either to very great overcharge (2.292) or very great undercharge (1.708), respectively, for the intervening oxygens, as listed in Appendix B, Table B1, Model L. The overcharge or undercharge is significantly reduced if one or more disordered layers are placed between the ordered A and ordered B domains. This brings the overcharge next to an ordered Ti layer down to 2.146 and the undercharge next to an ordered Fe^{2+} layer up to 1.854 as listed in Appendix B, Table B1, Model M, however, the situation is far from satisfactory.

Either Fe-rich contact layers, or Ti-rich contact layers, can be inserted between ordered Fe layers or ordered Ti layers and disordered layers, to improve the situation more. Fe-rich contact layers would be partially ordered layers that are an average of ordered Fe-layers and disordered layers with the composition $X = 0.60$, thus having the composition $Ti^{4+}_{0.19}\ Fe^{2+}_{0.41}\ Fe^{3+}_{0.4}$. Ti-rich contact layers would be partially ordered layers that are an average of ordered Ti-layers and disordered layers with the composition $X = 0.60$, thus having the composition $Ti^{4+}_{0.41}\ Fe^{2+}_{0.19}\ Fe^{3+}_{0.4}$. Either of these two kinds of contact layers have equal effect in reduction of charge imbalance down to 2.072 or up to 1.926, (Appendix B, Table B1, Model N). The same is true when bond-valence calculations are included (Appendix B, Table B2).

Note that in the Monte Carlo simulations of contact layers between haematite and ilmenite (Harrison 2006), only Fe-rich contact layers resulted. These simulations involved both chemical and magnetic interaction parameters, whereas the chemical ordering of composition $X = 0.60$ takes place entirely above the T where magnetic interactions are significant. However, examination of the purely chemical interaction parameters (K) given by Harrison (2006) provides significant insight. The strongest parameter at –2418 K is the one that lowers G by placing Fe^{2+} and Ti^{4+} in adjacent octahedrons across shared octahedral faces of adjacent (001) layers. It is this parameter that can drive both the Fe–Ti ordering process under either stable or metastable conditions and chemical phase separation of ilmenite and haematite under equilibrium conditions. By contrast, the parameter at +420 K is the one that raises G when Fe^{3+} and Ti^{4+} are placed in adjacent octahedrons within the same (001) layer. When nature makes a choice between Fe-rich and Ti-rich contact layers, this parameter acts strongly against Ti-rich contact layers and in favour of Fe-rich contact layers, even although charge balance considerations give nearly identical results. The improbable Ti-rich contact layers are hence dropped from further consideration

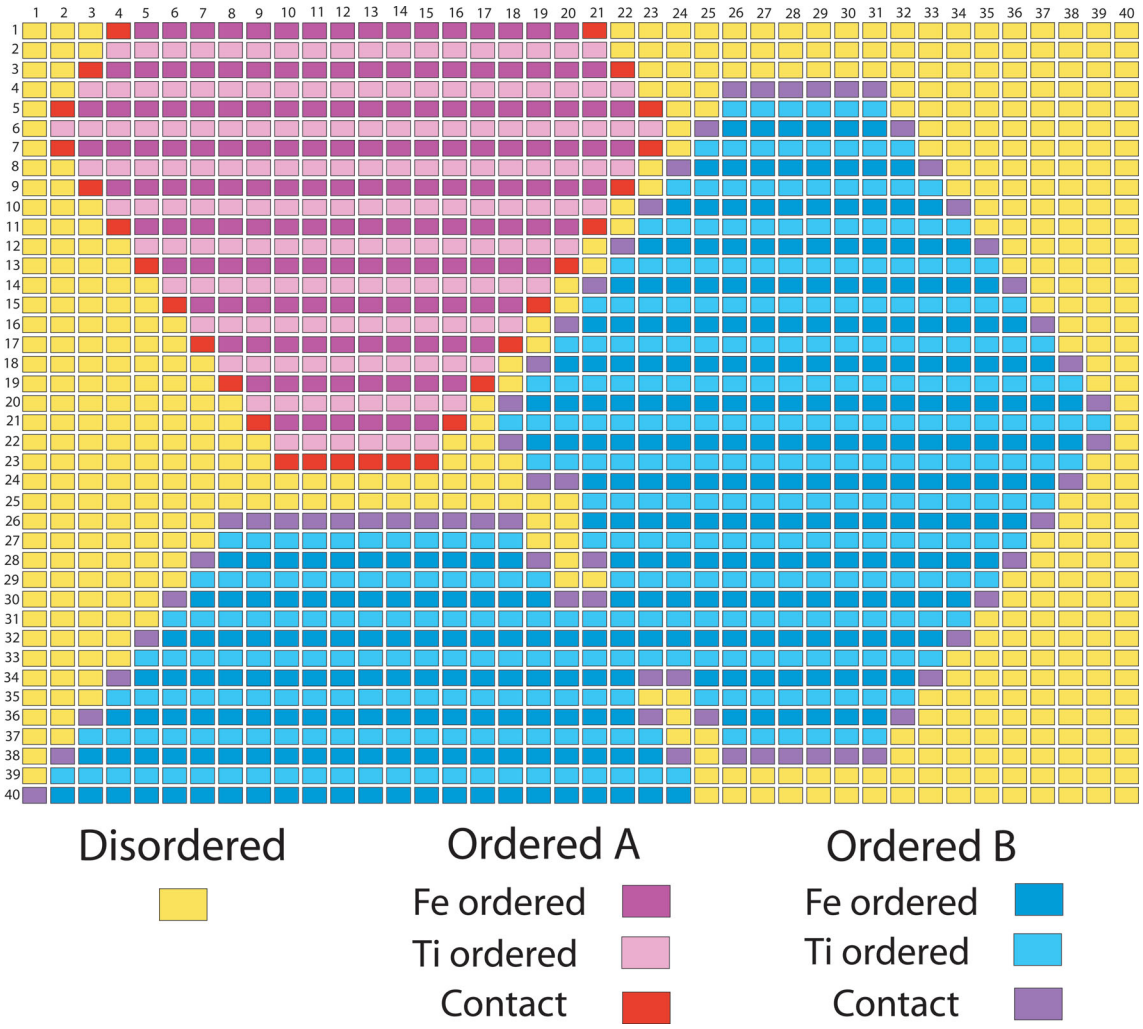

Figure 5. Schematic block model for composition $X = 0.60$ showing schemes for growth and interface configurations for ordered A and ordered B regions in a disordered matrix (see text). Horizontal rows are parallel to (001).

and only layer configurations involving Fe-rich contact layers are used.

Fe-rich contact layers, at interfaces between disordered and ordered phases, must, by definition, be placed adjacent to ordered Ti layers in the ordered phase, the same as they are adjacent to Ti-layers of ilmenite. An interesting outcome of this requirement is that when ordered A and ordered B domains occur across an (001) interface, the interface must consist of two contact layers and two disordered layers, or if the interface region is thicker, some even number of disordered layers. By contrast, when two ordered A domains or two ordered B regions occur across an interface, the interface would consist of two contact layers and only one disordered layer, or, if the interface is thicker, by some odd number of disordered layers. Alternatively two ordered A or ordered B regions might merge so that there would be zero contact layers and zero disordered layers.

Fig. 5 is a schematic model based on composition blocks within average composition $X = 0.60$, that shows growth and interface configurations of A-ordered domains (pink and magenta with red Fe-contact layers) and B-ordered domains (light and dark blue with violet Fe-contact layers) in a disordered matrix (yellow). The model consists of 1600 blocks, each one cation layer thick, and each of which may consist of one of seven compositions as indicated by their colour. All block types of Fig. 4 are used except Ti-rich contact layers. The diagram illustrates three ordered 'lamellae', one A-ordered and two B-ordered. One of the B-ordered lamellae is shown with a complete thickness (top to bottom) of 35 layers, which at 0.23 nm per layer, corresponds approximately to the 8 nm maximum thickness of ordered regions detected in our synthetic sample (Fig. 1). Starting either at the left end of the A-ordered region, or the right end of the large B-ordered region, the model can be used to illustrate growth steps to produce order from disorder. Each lamella is initiated in a three-layer reaction by creating one ordered Ti layer and two Fe contact layers from three disordered layers. Thereafter, the lamellar growth continues in a different three-layer reaction by creating one ordered Ti layer, one ordered Fe layer and one contact layer from one contact layer and two disordered layers. These reactions take place as a result of simple short-distance hopping of Fe^{2+} and Ti^{4+} ions between adjacent layers, as illustrated in Appendix C. This simplicity of movement is what allows ordering to proceed partially during quench from above the ordering T. When the growing ordered A and ordered B domains converge on each other perpendicular to (001), their closest convergence, based on most favourable charge balance considerations, occurs when they are still separated by two disordered layers and two contact layers. Further, their separations in the vertical direction perpendicular to (001) must always be by an even number of disordered layers. By contrast, when two growing B-ordered domains converge, they can merge, but if they remain separated, then their separations perpendicular to (001) must always be by an odd number of disordered layers.

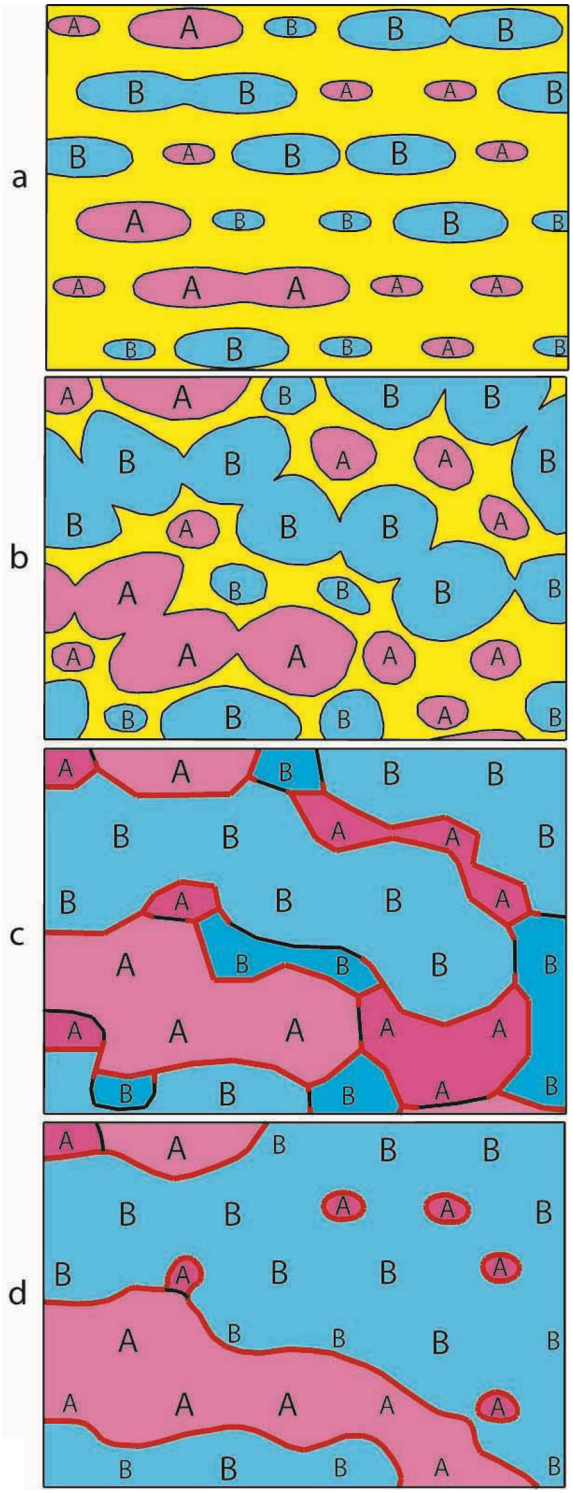

Figure 6. Progressive cross-sections of composition $X = 0.60$. (a) Nucleation and initial growth of A- and B-ordered domains in a disordered host. (b) Rapid expansion of larger ordered domains and slower expansion of smaller ordered regions into disordered host. (c) Converged ordered regions separated by antiphase domain boundaries in red. Synphase boundaries (see text) shown in black. Fe enrichment is shown by darker red and blue colours in smaller ordered regions. (d) Coarsening of large domains at expense of small domains by movement of antiphase domain boundaries.

7 SPATIAL CONCEPTS FOR GROWTH OF ORDER AND SUBSEQUENT COARSENING

Fig. 6 illustrates a generalized progression involving initation and growth of ordered regions in a disordered host, followed by near total elimination of disorder and movement of boundary regions to coarsen the intergrowth. The illustrations are stylized geometrically as compared to what would occur in nature, but this simplification makes it possible to illustrate these states in terms of block models.

Fig. 6(a) shows A- and B-ordered domains isolated in a disordered host. Both A- and B-ordered domains are shown in two sizes, larger ones, which formed earlier, and smaller ones, which formed later and have grown less. Their general distribution is somewhat random but in natural examples both their size distribution and spacing would likely be more irregular.

In Fig. 6(b) the ordered domains have grown. The larger regions grow more rapidly because of their larger surface area, so that compatible A and B domains have merged, although the pattern of earlier round shapes is still preserved. The smaller regions grow slower and none are yet merged.

In Fig. 6(c) the merging has proceeded completely, although the history of big and small domains is still in evidence. All boundaries between A and B domains are now chemical antiphase domain boundaries marked in red. Of particular importance for this view is that during expansion of the large ordered domains (see later), the Fe^{3+} content is swept into the small ordered domains. Although these domains have the same phase of chemical ordering, they differ at least temporarily in their Fe^{3+} content, and thus in their magnetization T. To keep these important features in sight, we have named these chemical 'synphase' boundaries (marked in black).

Fig. 6(d) shows a further stage of coarsening in which the small ordered regions are in the process of elimination in favour of the larger ordered regions. In all probability, the synphase chemical distinctions are also in process of elimination in favour of larger more homogeneous domains of ordered phases, thus greatly reducing the extent of antiphase boundaries.

8 BLOCK ILLUSTRATIONS AND MOBILITY OF PHASE INTERFACES

Our next stage of evaluation is to consider block models prepared for detailed simulation of the textural stages of Fig. 6. To do this we employed a field of 6400 blocks. Each block is a 2-D schematic representation of the contents of a part of a single cation layer 0.23 nm thick parallel to c, and extending approximately 0.45 nm along the (001) basal plane. This modelling is a compromise. Blocks of the size indicated are actually too small along (001) to contain a correct mix of atoms to cover the complex chemistry intended. At the same time the models are too small to show the numbers of layers probably involved. For example, Harrison *et al*. 2005 suggested an upper limit of 50 nm for antiphase domains involved in magnetic self-reversal, whereas the total thickness of the models is ∼18 nm. Using 6400 blocks we have produced instructive images in Fig. 7 representing the arrangements in Figs 6(a)–(d). In the colour scheme, lighter colours inside ordered regions (pink and light blue) represent Ti-ordered blocks. These occur commonly on the tops and bottoms of lamellae sandwiched between contact layers (red

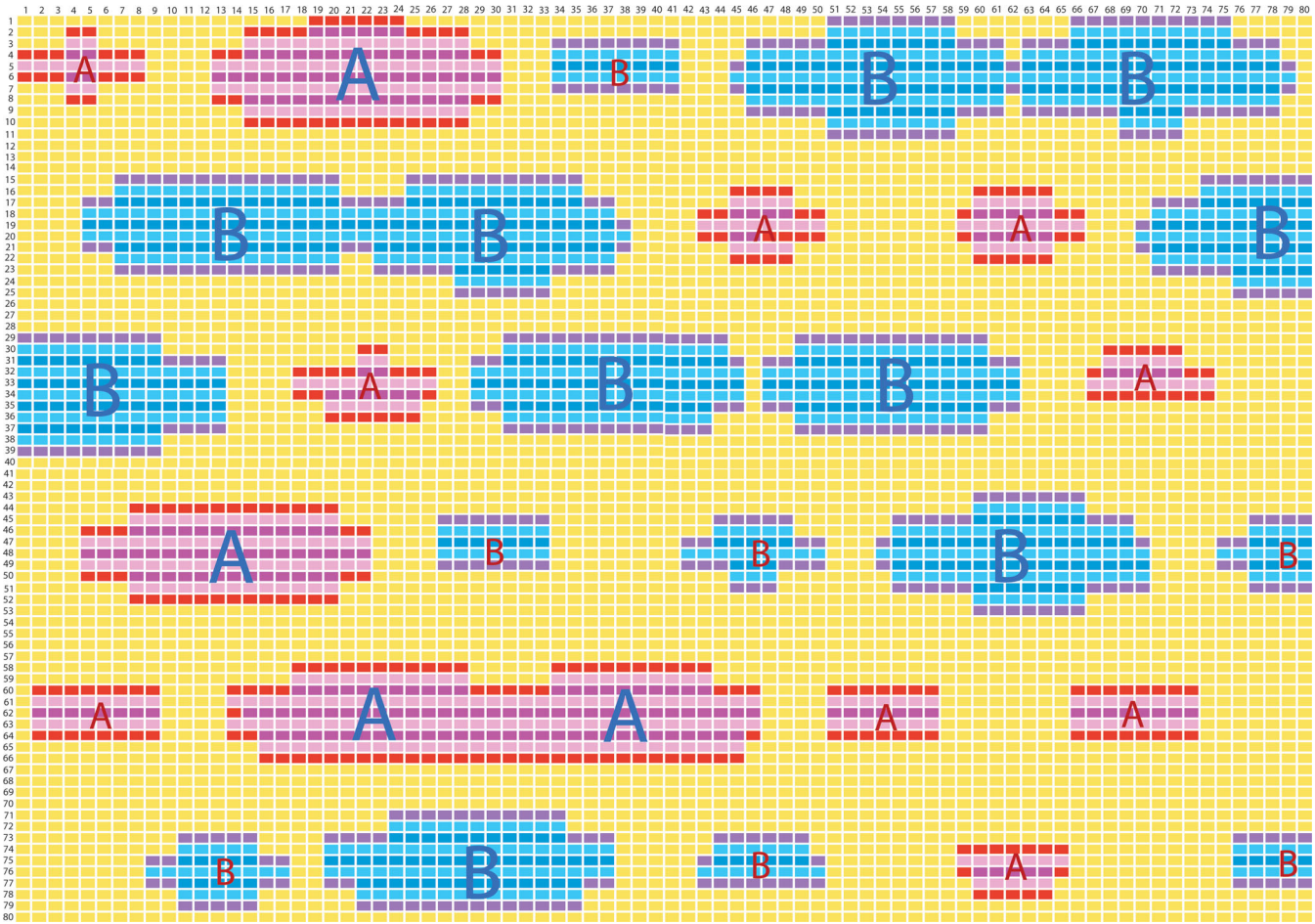

Figure 7. Colour block models illustrating the configurations of Fe-ordered, Ti-ordered, contact and disordered layers in the context of phase relations in Figs 6(a)–(d). Same colour key as Fig. 5. Synphase boundaries marked in black. (a) All ordered domains are separated by significant disordered regions shown in yellow. The larger A- and B-ordered lamellae do contain abundant magenta and dark-blue Fe-ordered layers, but these are scarce in smaller ordered domains where contact layers dominate. This figure continues over the next three pages (Figs 7b–d).

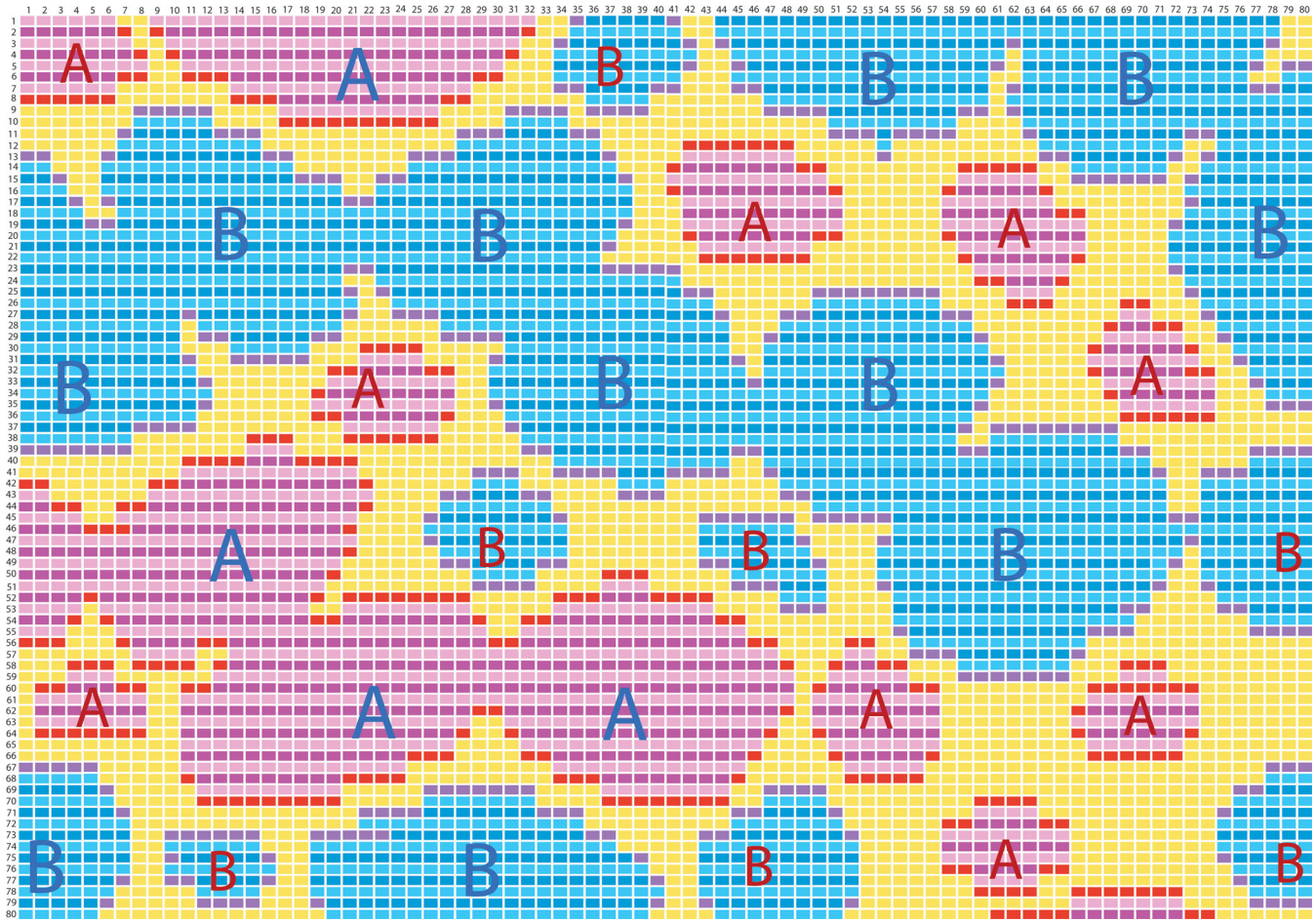

Figure 7. (b) Larger A- and B-ordered regions have grown more than smaller ordered regions. Compatible A and B domains have merged. Smaller regions have grown more slowly, and none are yet merged.

and violet, respectively). Fe-ordered layers (magenta and dark blue, respectively) only occur deep within the lamellae.

In Fig. 7(a) all ordered domains are separated by significant disordered regions in yellow. The larger A- and B-ordered lamellae do contain abundant magenta and dark blue Fe-ordered layers, but these are quite scarce in the smaller ordered domains where contact layers dominate. These model blocks create angular patterns and lamellae that are thinner than are likely in nature.

In Fig. 7(b) larger A- and B-ordered regions have grown more rapidly than smaller ordered regions because of their larger surface area. Compatible A and B domains have merged, although the pattern of earlier round shapes is still preserved. Smaller regions have grown more slowly and none are yet merged. Extensive areas of disordered phase are still preserved.

In Fig. 7(c), all disordered regions have been eliminated except for the two disordered blocks that are required along (001) of every antiphase domain boundary. Synphase boundaries are marked in black. These occur where small A regions postulated to be enriched in Fe (note darker red shades) are in contact with larger A regions, or where small B regions, also postulated to be enriched in Fe (note darker blue shades), are in contact with larger B regions. The most impressive feature here is the constant decoration of antiphase boundaries with both red and violet contact layers and two yellow disordered layers. Comparison of this image with the images in Figs 3, 7 and 8 of Nord & Lawson (1989) demonstrate that these boundary regions with two contact layers and two disordered layers are the regions that migrate back and forth through phase space as the coarsening process proceeds.

Fig. 7(d) illustrates a stage towards elimination of the small ordered regions in the midst of and along the edges of the larger ordered regions. The continuing objective of this process is the decrease in energetically unfavourable boundary regions and the development of larger and larger domains of ordered phases until chemical antiphase domain boundaries are ultimately eliminated.

9 MODELS FOR CHEMICAL EVOLUTION DURING QUENCH AND ANNEALING

9.1 Background

The composition data in Paper I (Fabian *et al*. 2011, especially fig. 7), demonstrating chemical phase separation, have been used to try to understand the chemical changes in the $X\mathrm{Ilm} = 0.61$ sample during quench from the annealing T at 1055 °C (1328 K) above the Fe–Ti order transition, and during subsequent annealing below that transition.

The data are only from the quenched sample, before subsequent annealing. The relative intensities of TEM diffraction spots suggest that the sample consists of ∼0.46 volume fraction of ordered phase

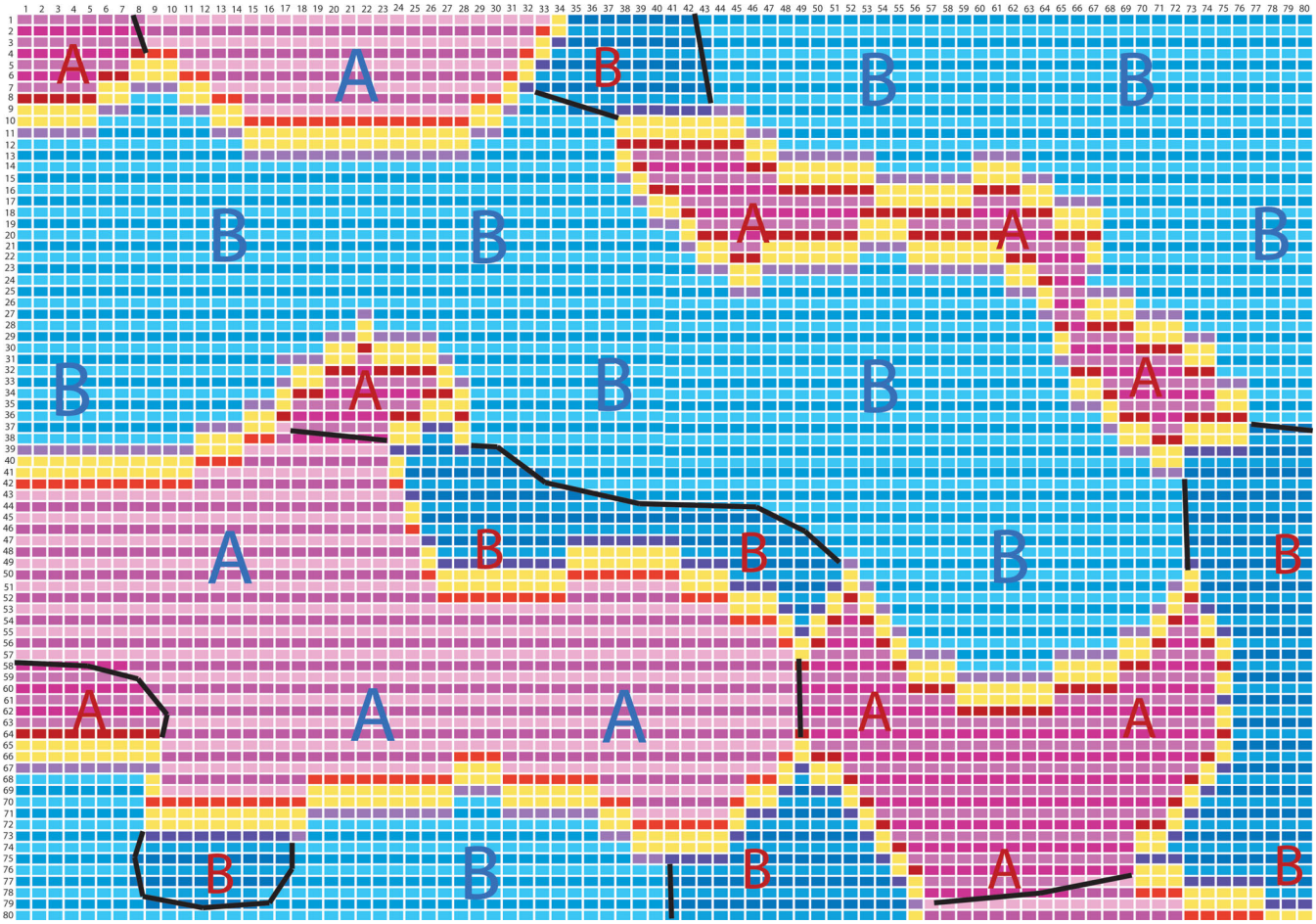

Figure 7. (c) All disordered regions eliminated except for two ordered blocks required along (001) of every antiphase domain boundary. Synphase boundaries marked in black occur where small A regions postulated to be enriched in Fe (note darker red shades) are in contact with larger A regions (or vice versa). Antiphase boundaries are decorated with both red and violet contact layers and two yellow disordered layers.

and ∼0.54 volume fraction of disordered phase. Measurements of Mrs versus T, showed that the majority of the ferrimagnetic ordered phase ranges in composition from $X = 0.61$ to 0.64. Measurements of Ms versus T suggest that the majority of the antiferromagnetic phase does not extend in composition below $X = 0.56$. These comments apply to the most abundant material responsible for magnetic properties. A small number of Ti-rich analyses extends to $X = 0.70$ and Fe-rich analyses to $X = 0.50$. When the value of 0.605 is used to divide the TEM–EDX analyses into two groups, those above 0.605 account for 0.46 (fraction) of the analyses whereas those below account for 0.54 (fraction). These values are similar to the TEM abundance estimates and can be used during consideration of T–composition phase diagrams.

The quenched sample $X = 0.61$ showed neither self-reversed thermoremanent magnetization nor room-T magnetic exchange bias. The requirements for magnetic self-reversal (Uyeda 1958; Ishikawa & Syono 1963; Nord & Lawson 1989) are to have one phase with a higher magnetization T (hence more Fe-rich) magnetically coupled to an oppositely ordered phase with a lower magnetization T. It is not required that the phase with the lower magnetization T be in the majority, only that it dominates after being magnetized. In Paper I we showed that these requirements were achieved in our sample by short-term heating of the sample under conditions allowing growth of A- and B-ordered regions until they became the major phase.

9.2 T–composition phase diagrams

The two best-developed phase diagrams are those of Harrison (2006; Fig. 8a) and Ghiorso & Evans (2008; Fig. 8b). Both show a tricritical point, the existence of which was explained earlier by Burton (1982, 1985, 1991) and Burton & Davidson (1988). Figure 8(a) shows the disorder to order transition as a single line down to the tricritical point at 1065 K and $X = 0.57$, with equilibrium phase separation towards widely separated compositions only below this T. Figure 8(b) shows one of the three thermodynamically consistent versions given by Ghiorso and Evans. Here the tricritical point is shown at higher T and more Ti-rich composition, and there is an extensive narrow loop with parallel Fe enrichment of both ordered and disordered phases, extending towards lower T, before the equilibrium ordered phase eventually turns towards higher Ti content. Here we have added dashed lines, not thermodynamically based, representing possible locations of chemical spinodals (see Appendix D).

The route to understanding the diagrams of Fig. 8 begins with Fig. 2, illustrating the relationship between G and the Fe–Ti order parameter Q. It is drawn for a single value of $X FeTiO_3$ and a single T below the disorder to order transition for this composition. Here the two binodes (B) represent the equilibrium ordered and anti-ordered values under these conditions, with complete disorder ($Q = 0$) represented by a much higher G. In between the binodes lie the spinodes (S), inflection points on the curve. Between the spinodes, disordered phases can evolve towards more order by spinodal

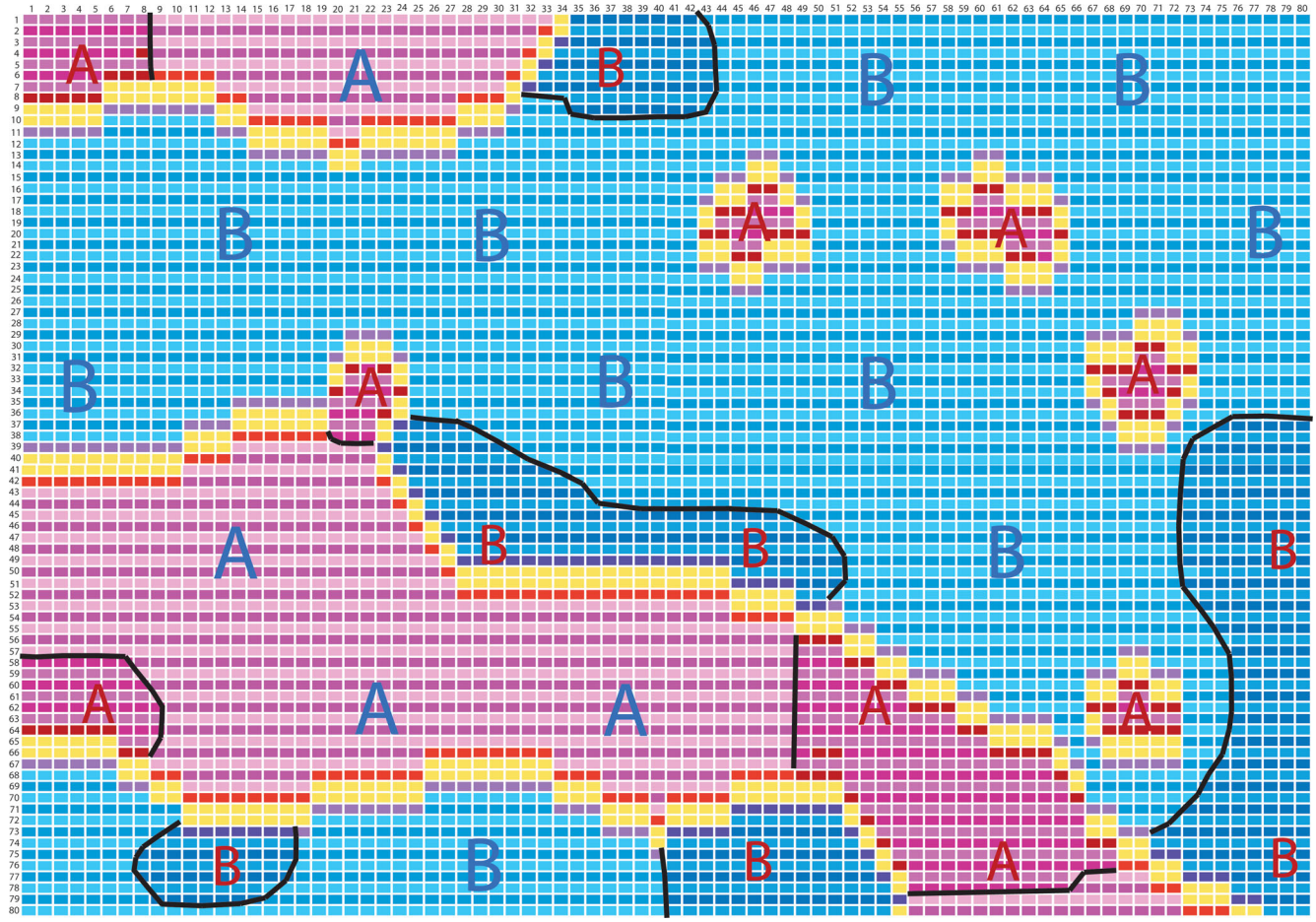

Figure 7. (d) A stage toward elimination of small ordered regions in midst of and along edges of larger ordered regions.

decomposition, spontaneous development of more order and anti-order without requirement for nucleation.

Families of curves like the one in Fig. 2 can be generated, representing G for different values of $X\mathrm{FeTiO_3}$ at constant T. We know from experimental and theoretical studies that an increase in $X\mathrm{FeTiO_3}$ will open up the gap between equilibrium ordered and anti-ordered phases, giving both higher positive and higher negative values of Q. Similarly, we know that a decrease in $X\mathrm{FeTiO_3}$ will cause the gap to narrow, eventually reaching zero width at the equilibrium disorder to order transition for that T. At still lower values of $X\mathrm{FeTiO_3}$ there will be no stable ordered phase and the G versus Q curves will be simple convex downward curves with G minimum at $Q = 0$.

Fig. 9(a) is a schematic assembly of a series of G versus Q curves for different values of $X\mathrm{FeTiO_3}$ at a single T. This creates a 3-D surface with Q ranging from –1 to +1 and $X\mathrm{FeTiO_3}$ within the range of interest, approximately 0.40–0.80. The central solid black line indicates the G of completely disordered phases, stable for compositions left of the disorder to order transition and metastable for compositions to the right. The solid red line indicates stable ordered and anti-ordered phases diverging '+' and '–' from the disordered line, beginning at a critical point. The dashed red line indicates the traces of the inflection points of the G–Q curves. We here call these Q-spinodal lines, distinct from chemical-spinodal lines occurring at lower T. The Q-spinodal curves necessarily converge at the critical point of the stable disorder to order transition. The critical point has the special property of zero curvature in the G–Q direction, although no change in the sign of curvature in the G–X direction.

The region outlined by the spinodal lines in Fig. 9(a) has special importance when considering reactions during quench from high T. During this process the fixed bulk composition passes successively through a family of surfaces similar to Fig. 9(a) with the disorder to order point moving successively towards lower values of $X\mathrm{FeTiO_3}$. Because equilibrium cannot be maintained, any disordered composition will enter the region where spinodal ordering will ensue. Inside this region, a single disordered phase (red dot) will have a higher G than combinations of two partially ordered phases, plus a disordered phase of lower $X\mathrm{FeTiO_3}$ (coloured triangles). The special metastable arrangements of these triangles is a consequence of the very strong tendency for Ti enrichment in the ordered versus the disordered phase, as outlined in Section 5 and illustrated in Fig. 3. It can occur under T conditions where there is no chemical phase separation related to a stable disorder to order transition. It plays a key role in the early development of quench microstructures as considered here, and can occur over a wide range of compositions.

Progressive metastable evolution from disorder, represented by the red dot, towards greater order is shown by the series of triangles, each representing lower G. In the orange triangle, the minority ordered phases have formed by spinodal decomposition, but still lie within the spinodal region between the Q-spinodal lines. In the green triangle, the more abundant ordered phases lie exactly on the Q-spinodal lines, although only coincidentally. The blue

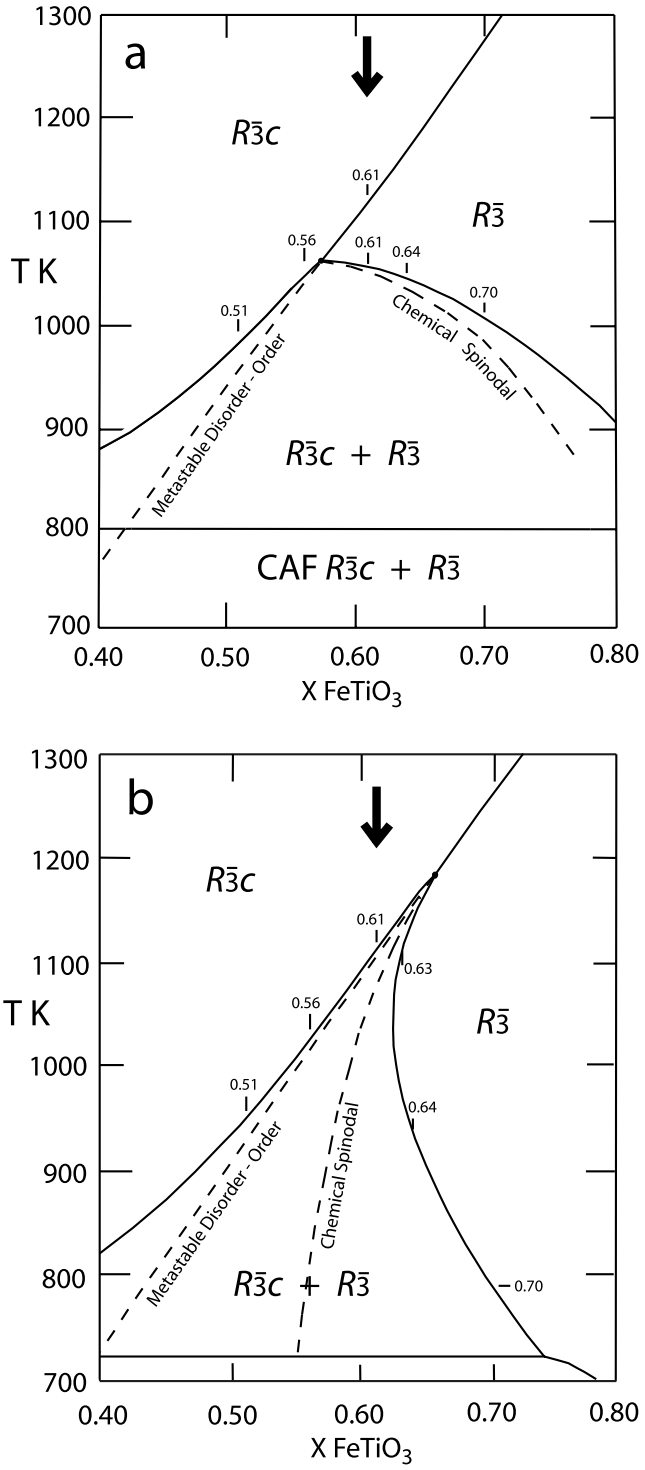

Figure 8. Calculated phase diagrams of (a) Harrison (2006) and (b) Ghiorso & Evans (2008) with approximate spinodal boundaries added.

triangle illustrates the fact that once ordered phases are initiated spinodally, they can move towards greater order outside the spinodal region, at the same time consuming more of the disordered phase, and can ultimately reach an equilibrium degree of order on the binodes.

The coloured triangles in Fig. 9(a) show that, as ordering proceeds, the proportions of ordered versus disordered material change and hence, by the lever rule, the compositions of the phases must adjust. As ordering proceeds, the proportion of disordered phase decreases because of coarsening and, therefore, the compositions of the ordered and anti-ordered phases move closer to the original bulk composition. Taken to its logical and thermodynamically correct conclusion, that is, equilibrium at a T above the tricritical point, the result would be a homogeneous ordered Ilm61 with no disordered boundaries. The compositional heterogeneity will only be preserved if quenching prevents the transition to long-range order from occurring before the tricritical point is reached. Once below the tricritical point, (see later) annealing can enhance the trapped composition differences, because equilibrium then involves disordered and ordered phases with different compositions. The key difference between these stages is that above the tricritical point the compositional heterogeneities are a transitory solution to minimising the G, below the tricritical point they are a stable solution.

At lower T than illustrated in Fig. 9(a), a new feature appears. This is the development of a separate G minimum in G–X profiles of the G surface of the ordered phase as illustrated in Figs 9(b) and (c), and two new inflection lines which are chemical spinodes on the G surface of the ordered region. This leads, through a critical point, to equilibrium chemical phase separation of disordered and ordered phases illustrated by the black triangle in these figures. This development of the G surface creates a line of minima (solid blue connecting blue binodes) along the ordered-phase surface and two lines (dashed blue connecting blue spinodes) representing inflection points in profiles along the G–X direction. These blue lines approach, but never reach, the central line of the diagram where $Q = 0$ and order has no influence.

To get from the configuration of Fig. 9(a) to that of Figs 9(b) and (c), one must pass through the tricritical point as shown on Fig. 8(a). The nature of this tricritical point was illustrated in G–X sections by Allen & Cahn (1976a,b). Their drawing, with appropriate modification to fit Fig. 8(a), is shown in Fig. 10. The disordered and ordered curves meet in tangency at the disorder to order transition. As soon as a dimple appears in the curve of the ordered phase, then there are two spinodal points, one coinciding with the disorder to order transition, and the other, closer to the stable ordered phase, which can be called the chemical spinodal. By this stage, the stable ordered phase has a composition right of the disorder to order transition, and the transition itself is metastable. The tricritical point itself, which is unique to T, has very special properties. It represents a point where the inflection points on G–Q sections converge on each other. It also represents a point where the inflection points in the G–X section of Fig. 10 converge on each other. Thus, the curvature of the surface is zero in both directions. Metastability of the disorder to order transition ends under conditions where the equilibrium black tangent triangle in Figs 9(b) and (c) converges from a triangle to a single point, which is the tricritical point.

The features of Figs 9 and 10 can also be reconstructed to agree with the phase diagram of Ghiorso & Evans (2008) in Fig. 8(b). The main difference is that equilibrium phase separation begins at higher T with a higher T tricritical point. In addition, the equilibrium limb of the ordered phase initially changes composition towards higher Fe content, then changes slope at lower T so that the ordered phase becomes more Ti rich. At the outset it seemed that the high-T stable binary loop provided by the Ghiorso and Evans diagram would be essential to generate the chemical phase separation required to explain the quench features found in a wide range of compositions. However, the construction and interpretation of Fig. 9(a) shows that chemical phase separation driven by phenomena in the Q-spinodal region can provide all the needed impetus for small-scale

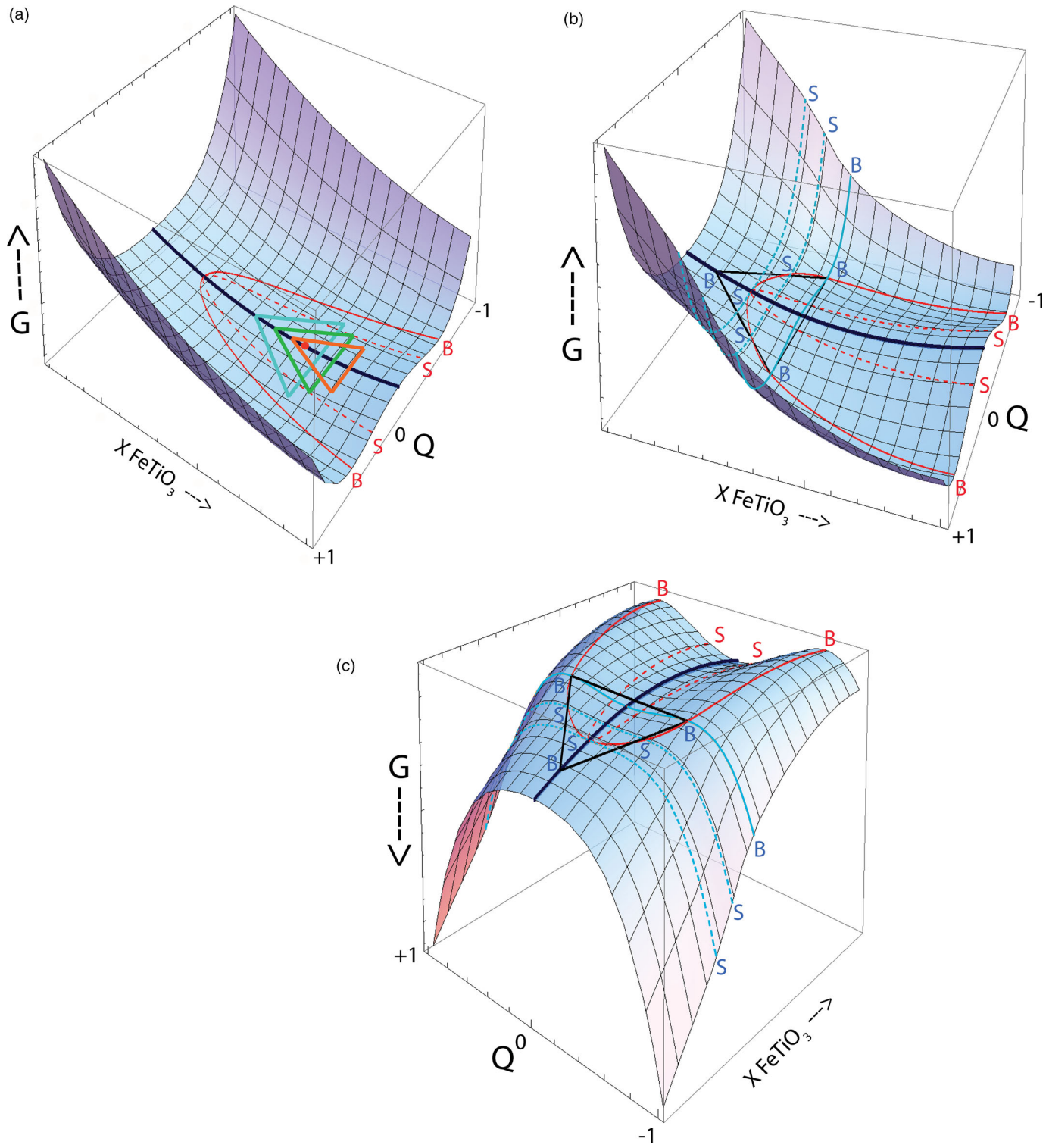

Figure 9 Qualitative surfaces of Gibbs free energy as a function of Q and $X\mathrm{FeTiO_3}$ to explain disorder–order phase relations as illustrated in Fig. 8(a) and derivative from features in Fig. 2. (a) Surface for conditions at T higher than the tricritical point, in normal view. (b) Surface for conditions at T below the tricritical point in normal view. (c) Surface for the same conditions but in inverted view. Red B and S are points on Q-binodal and Q-spinodal traces respectively. Blue B and S are points on chemical bimodal and chemical spinodal traces, respectively.

separation over a wide range of compositions all above the tricritical T. This can be followed at late stages of quench, or during subsequent annealing, by features where compositions can move closer to the equilibrium chemical solvus. The chemical phase separation in quench provided by the Q-spinodal region is not easily portrayed, except schematically, on the G–X section of Fig. 10. However, the G–X trace of the Q-spinodal can be shown, and is an addition to the equilibria illustrated by Allen & Cahn (1976b).

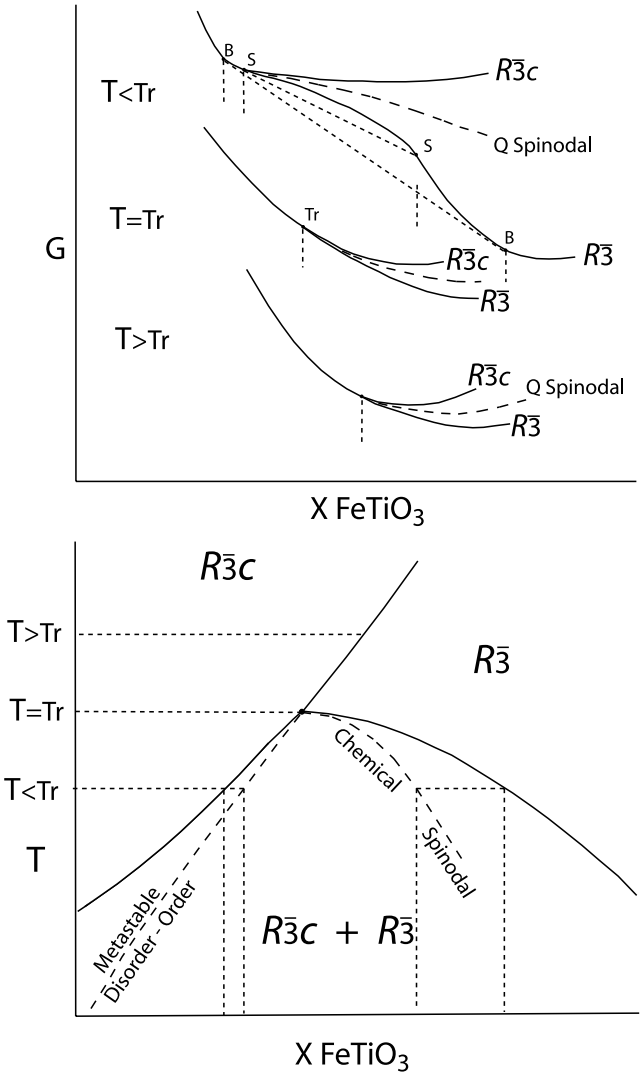

Figure 10. Phase relations around a tricritical point and a related set of G versus composition diagrams for different T's illustrating spinodal effects. Modified from Allen and Cahn (1976b) for the tricritical point (Tr) of haematite–ilmenite system shown in Fig. 8(a). Chemical spinodal boundary is as in the original. Q-spinodals are derived from the relations illustrated in Fig. 9.

9.3 Chemical evolution and chemical migration during coarsening

The evolution of disorder to order, and chemical phase separation provided by metastable and stable phase relations during quench and subsequent annealing involving both the Q spinodal and the chemical spinodal is illustrated in a sequence of parallel steps in Fig. 11. In (a), at T's below the critical T for cation ordering but above the chemical spinodal, sinusoidal fluctuations in Q develop spontaneously, resulting in alternating regions of order ($Q > 0$) and anti-order ($Q < 0$). Metastable fluctuations in X with exactly half the wavelength of those in Q are generated (see Figs 3 and 9a), so that disordered boundary regions are Fe-enriched with respect to ordered and anti-ordered regions. Growth of sinusoidal fluctuations in Q and composition continues in (b) and (c), enhanced in (c) with cooling below the tricritical T where the chemical spinodal comes into effect. Stages (a), (b) and (c) are closest to the features illustrated in Figs 1, 6(a), (b) and 7(a) and (b). In (d) well-defined ordered and anti-ordered domains with disordered boundaries and contact layers are achieved by short-range diffusion. This stage is closest to the features illustrated in Figs 6(c) and 7(c). In (e) there is a partial transition from short-range to long-range order driven by a combination of lateral growth of the ordered domains, and a decrease in the degree of order within the anti-ordered domains. Loss of cation order and encroachment of the Fe-rich boundaries results in Fe enrichment across the entire anti-ordered domain (Harrison *et al*. 2005). This stage is closest to the features illustrated in Fig. 6(d) and 7(d). In (f), with prolonged annealing, an intergrowth of Ti-rich ordered and Fe-rich disordered phases is achieved. The wavelength of fluctuations in Q and X now match.

The composition distribution for the quenched sample (Fabian *et al*. 2011, Fig. 7) can be only qualitatively related to the phase diagrams of Figs 8–10, but appears to have been created in stages (a), (b) and (c) of Fig. 11. When first encountering the disorder to order transition, composition 0.61 decomposed by the Q spinodal, probably to a partially ordered composition near 0.64 plus a disordered phase with a composition 0.59 or less (Fig. 9a orange triangle). It is important to note that Fig. 9(a) represents a somewhat 'static' illustration whereas during real quench with rapidly falling T would be represented by a whole series of similar G surfaces racing from right to left across the bulk composition. In some locations there may have been no further reactions than the initial one, but in others equilibration would have continued (see green and blue triangles in Fig. 9a), locally to the point of exhaustion of the disordered phase, most likely with a composition close to 0.56, and creation of an equilibrium ordered phase of composition 0.61, which is abundant in our data set. Although it is difficult to quantify, we suggest that ordered compositions above about 0.64 and disordered compositions below about 0.56 were created in stage (c) during the last stages of quench, below the tricritical T, influenced by normal chemical spinodal phenomena, which are, in effect, initial stages of true exsolution. There is some chemical evidence to suggest that this final stage occurred by short-range chemical interactions along phase boundaries.

The most challenging aspect of the chemical evolution is related to the fact that the chemical boundaries move during the process of coarsening either during quench or during annealing after quench. The spinodal relationships described in T–Q–composition space must also be operative in real space so long as there is disordered material to be consumed, as outlined earlier. After total elimination of disordered phases, except those associated with contact layers, the phase boundaries continue to move. This is proved by the TEM images of Nord & Lawson (1989). One would like to see a detailed series of images showing the movement of chemical walls during evolution of the same material, but this is not yet possible. To gain a general concept, think of a region where B-ordered domains are coarsening relative to A-ordered domains. The 2-D geometry of such a situation may be reasonably portrayed in the TEM image of Nord & Lawson (1989) Fig. 3(d), which is reproduced here as a tracing in Fig. 12 (top panel). In order for the coarsening to continue, the chemical walls marked by disordered or partially disordered material (yellow) are in general moving away (arrows) from the centres of B-ordered domains (blue) and towards the centres of A-ordered domains (red) in this image. The Monte Carlo simulations in Fig. 3 provide a convincing argument for Fe enrichment along the borders of the ordered regions (darker pink in Fig. 12 (bottom panel), that are shrinking as compared to those that are enlarging, as suggested in Harrison *et al*. (2005). The chemical profile in Fig. 11(e) illustrates very closely the chemical differences across

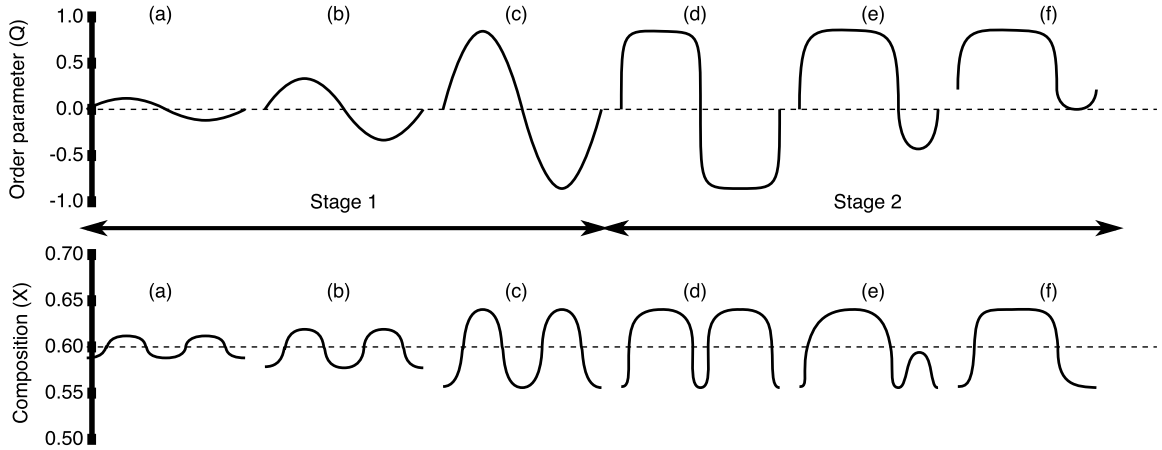

Figure 11. Conceptual model for the spatial and temporal evolution of the cation order parameter, Q (top), and chemical composition, X (bottom), during quenching of an initially disordered crystal with composition $X = 0.6$. The abscissa of each plot represents distance within the crystal (arbitrary length scale). T decreases and time increases from left to right.

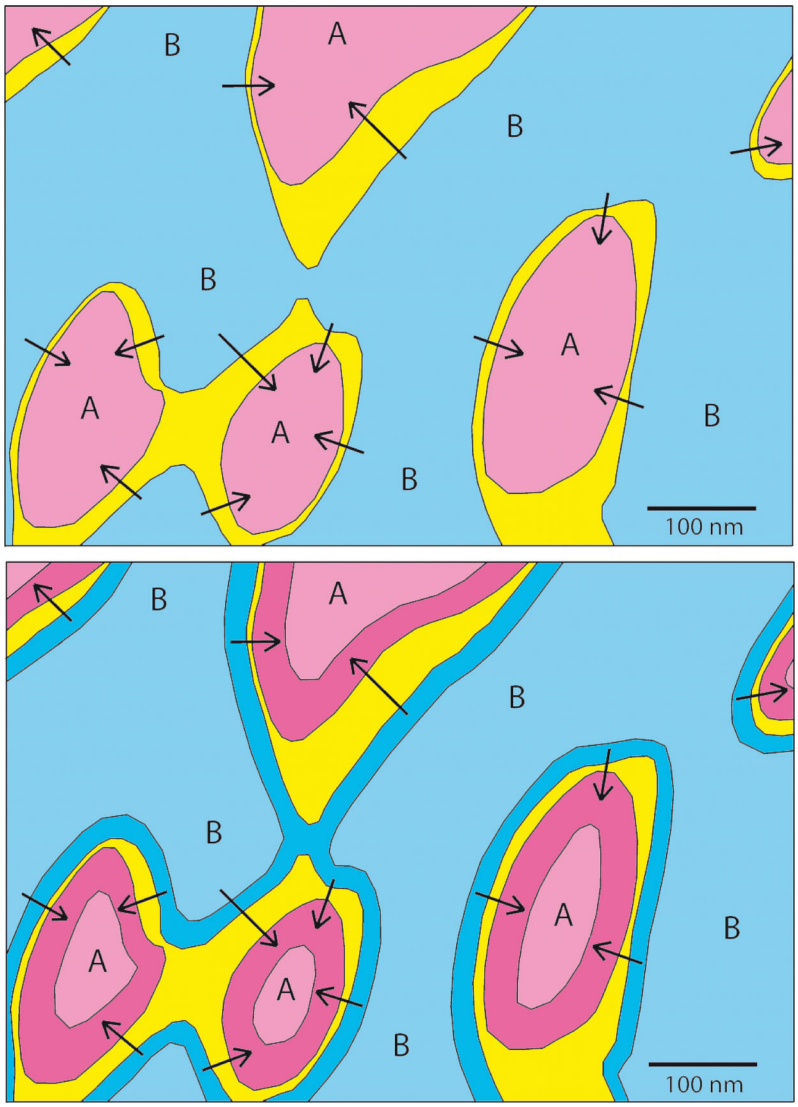

Figure 12. (Top) Tracing of Fig. 4(d) of Nord & Lawson (1989) illustrating enlargement of a B-ordered phase (blue) and diminishment of an A-ordered phase (pink). Continuation of this process requires movement of disordered (yellow) chemical domain boundaries indicated by arrows. (Bottom) There should be a region of Fe enrichment (darker red) on the boundaries of the diminishing A-ordered domains. Chemical changes (darker blue) along trailing edges of the boundaries within the enlarging B-ordered domains (Ti enrichment?) seem less probable.

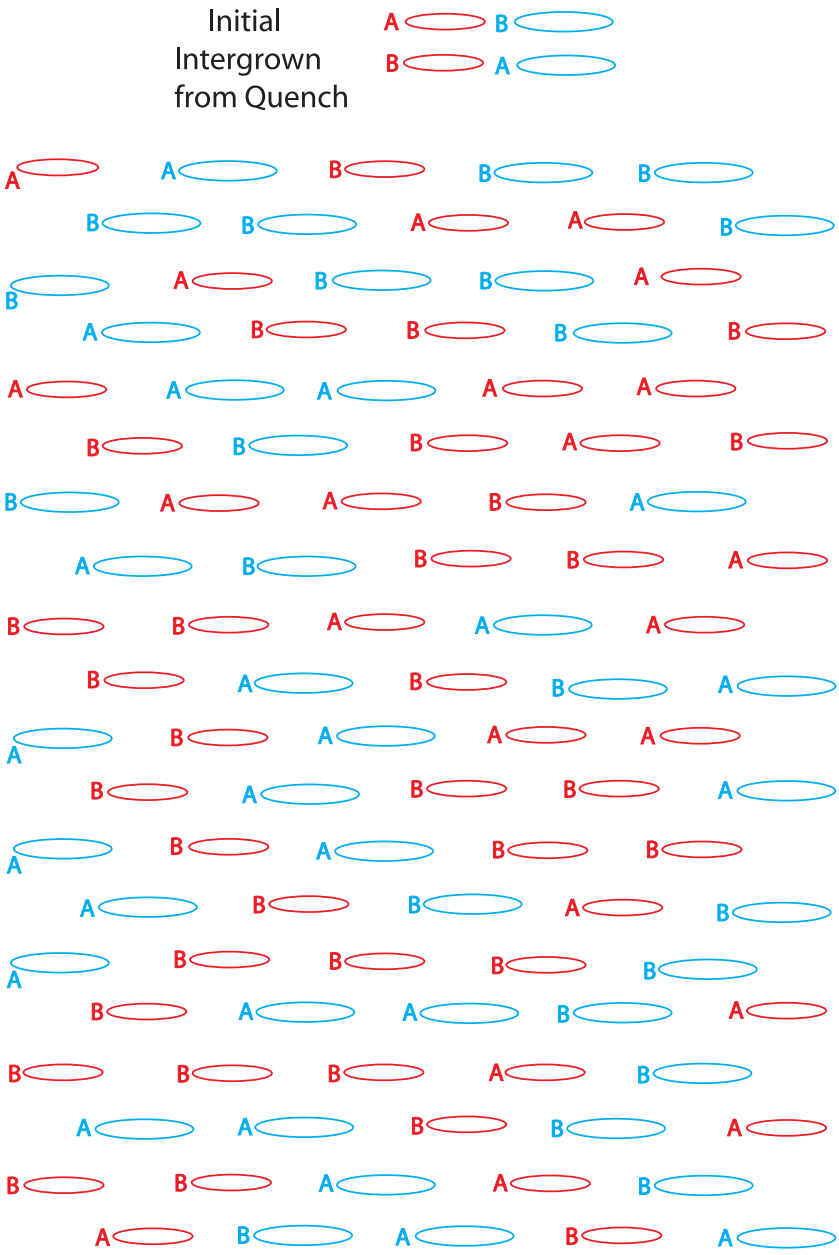

Figure 13. Schematic diagrams illustrating probable stages in chemical evolution of microstructures in an approximate $X = 0.60$ composition during quench and subsequent annealing. (a) Creation of a more or less random pattern of A- and B-ordered domains in a disordered matrix during quench. Red regions are slightly smaller than blue regions. This figure continues over the next two pages (Figs 7b and c).

an antiphase boundary suggested in Fig. 12 (bottom panel) It is less clear if there would be chemical differences such as greater Ti enrichment (darker blue areas) along the trailing edges of the moving boundaries.

9.4 Summary of chemical evolution

The Monte Carlo simulation and currently available phase diagram details can be combined with available chemical data to give a general concept of disorder–order transitions and phase separation. Metastable equilibria involving spinodal decomposition, as might be expected during quench, are more effective than stable equilibria in explaining the data. Metastable spinodal chemical phase separation can occur during quench in two regions, along Q spinodals at T above the tricritical point and along chemical spinodals at T's below. Q spinodals based on the Harrison phase diagram (Fig. 8a) have the best effect in explaining evidence for chemical phase separation over a considerable composition range and also provide the setting for metastable ordered phases of compositions XIlm 45–70 that can be preserved by slow kinetics within the region where exsolution is the stable process. The characteristics of the two kinds of spinodal regions illustrate the very local Fe enrichment in both ordered and disordered phases along phase boundaries, caused by partial equilibration during fast cooling. Such local composition change and local Fe enrichment appear to provide the necessary differences in Curie T's needed to obtain magnetic self-reversal. A fortunate feature in this composition range is that all chemical features are completely locked in at T's well above those where the phases become magnetized. This is a very significant difference from effects produced during exsolution of CAF haematite from

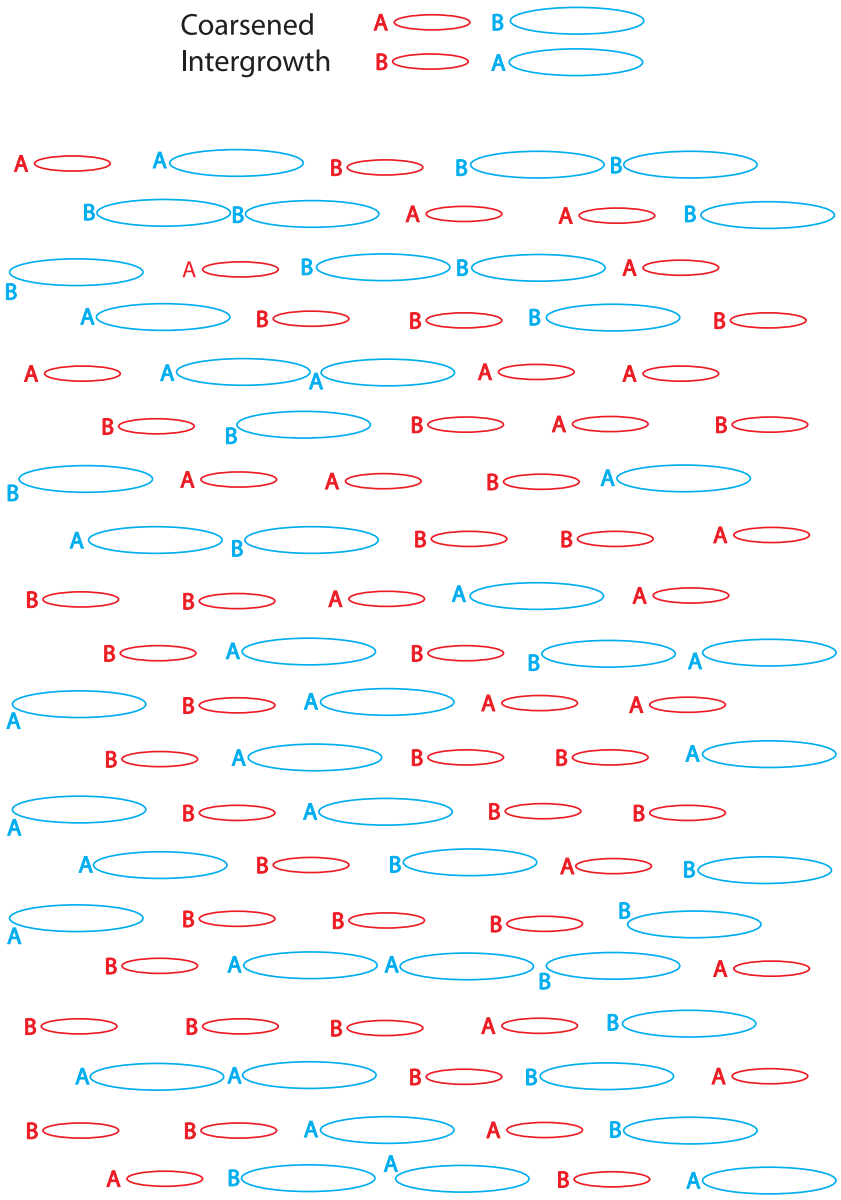

Figure 13. (b) A coarsened intergrowth of A-ordered and B-ordered regions still maintaining a disordered matrix. In coarsening during annealing, blue domains enlarge more rapidly than the red domains. The result is that some regions are dominated by large A-domains and small B domains, others are dominated by large B-domains and small A domains.

$R\bar{3}$ ilmenite, or vice versa, where the CAF haematite is below its Néel T during exsolution, so that magnetic properties can influence chemical evolution.

The coarsening experiments of Nord & Lawson (1989) demonstrate that the chemical domain boundaries migrate through the material during quench, or during annealing after quench. The spinodal relationships postulated on the phase diagram in chemical space appear to be operative also in real space until all the disordered phase is consumed. After that the domain boundaries migrate through the progressively coarsening material. The new Monte Carlo simulation provides convincing evidence for substantial Fe enrichment along the advancing edges of the boundaries as they move inwards towards the centres of those ordered regions that are diminishing in size.

Our overall notion of chemical growth, coarsening and chemical migration is encapsulated in the images of Fig. 13, which resemble parts of Figs 6 and 7 but in an expanded format useful for the magnetic models in Paper III. Fig. 13(a) shows a broad scattering of A- and B-ordered domains in a disordered space. Sizes and distributions of domains are nearly random but larger ones are indicated in blue and smaller ones in red. Such a distribution could be found after quench. Fig. 13(b) shows a partially evolved texture in which larger blue domains have become very much larger whereas smaller red domains are enlarged only slightly. Fig. 13(c) shows a much more evolved texture. During this evolution large blue A and B domains have expanded greatly whereas small red A and B domains have expanded only slightly to meet the large domains along red antiphase domain boundaries, providing for total elimination of the disordered phase except as required along the boundaries. Note the similarity of this pattern, achieved without any prior planning, to the patterns in TEM images of Nord & Lawson (1989). During this process the small red A and B domains have become

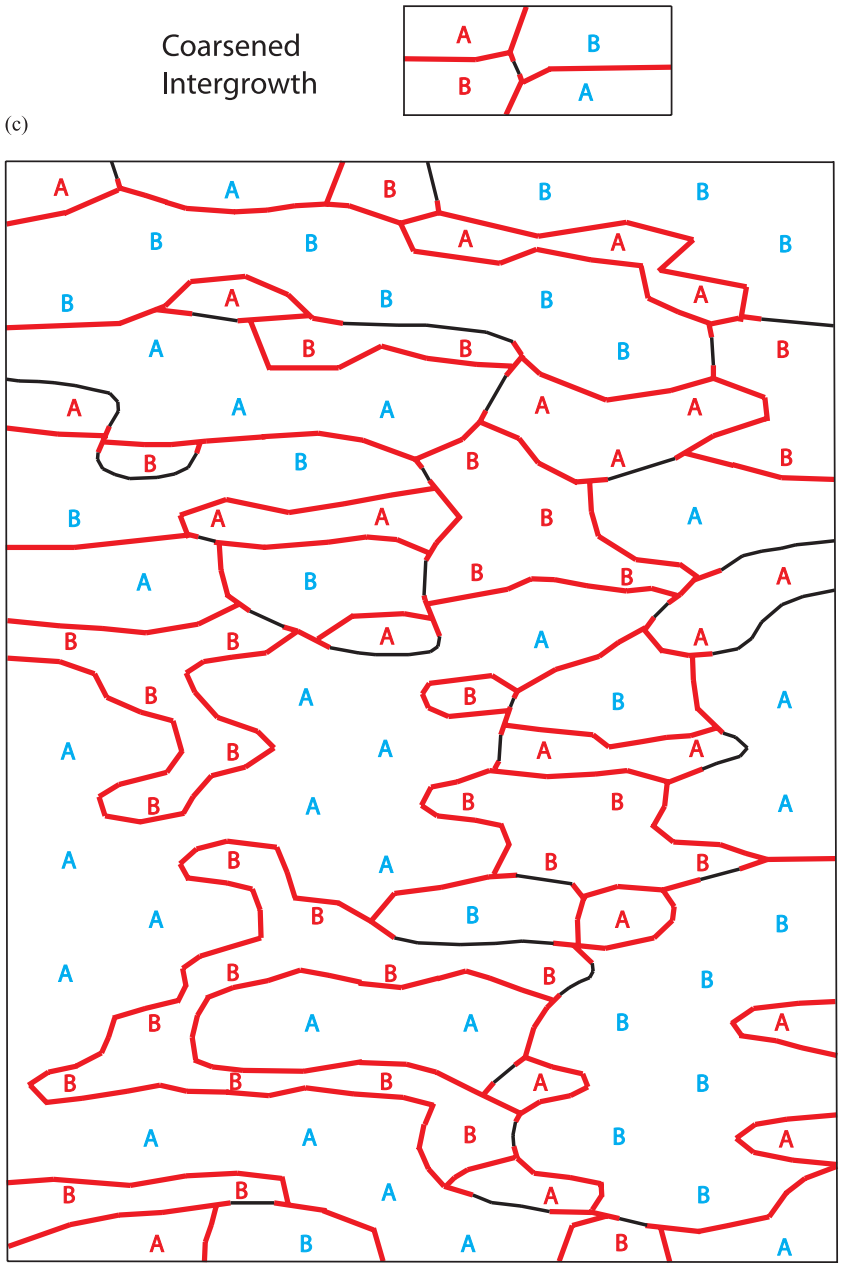

Figure 13. (c) Intergrowth has coarsened to the extent that all significant vestiges of the disordered phase have been eliminated except along very thin antiphase boundaries marked in red. Compare the pattern to those in TEM images of Nord and Lawson (1989). In addition there are a few special chemical boundaries marked in black between small A domains and large A domains, or between small B domains and large B domains. These boundaries indicate a difference in chemical composition between iron-enriched and less ordered diminished domains, and Ti-enriched and more ordered enlarged domains, even though the sense of chemical ordering is the same. These we call 'synphase' boundaries, and they have key properties in certain magnetic experiments.

enriched in haematite component compared to the larger blue A and B domains where the haematite component is slightly less. This chemical difference is indicated by black lines, here called synphase boundaries, along the contacts between small A-ordered and large A-ordered domains and between small B-ordered and large B-ordered domains. These boundaries become significant in magnetic interpretation.

Note that the whole of Fig. 13(c) can be subdivided into two kinds of areas: (1) where large A-ordered parts are dominant and small B-ordered parts are subordinate and (2) where large B-ordered parts are dominant and small A-ordered parts are subordinate. The significance to magnetic properties of this type of texture, produced by quench and later brief annealing, will be shown in Paper III of this series.

10 CONCLUSIONS

Paper I of this series gave magnetic and TEM observations and TEM–EDX chemical analyses on a synthetic sample with $X\mathrm{FeTiO_3} = 0.61$ in the $\mathrm{Fe_2O_3}$–$\mathrm{FeTiO_3}$ solid solution that had been quenched from 1055 °C above its Fe–Ti ordering T. Here we have explored details of chemical and textural evolution of this composition during quench and short-term annealing with these conclusions.

(1) Below the ordering T, a spinodal region is defined within which local fluctuations in Q initiate partially ordered and anti-ordered phases without requirement for nucleation. Transformation of disordered to ordered phases requires only local jumping of Fe^{2+} and Ti^{4+} ions between adjacent layers, compared to long diffusion distances for true exsolution.

(2) The driving force for Fe enrichment during ordering of ferri-ilmenite solid solutions is illustrated by 2-D Monte Carlo simulations. These depict ordering from a random state in a simplified Fe–Ti alloy, involving stability of atomic arrangements, particularly avoidance of Ti–Ti nearest neighbours.

(3) 'Contact layers', originally described for exsolved haematite and ilmenite to reduce interface charge imbalance, also play a role along the contacts of disordered and ordered phases of identical composition in microintergrowths produced during quench.

(4) Patterns of ordered, disordered, and contact layers in such microintergrowths and their evolution during quench and annealing are illustrated: (a) Random initiation of centres of A- and B-ordered domains in a disordered host, where all phase boundaries on (001) are decorated by Fe contact layers. (b) Earliest ordered domains grow fastest and largest, later ordered domains grow less. Large ordered domains of the same type merge, but where of different type, they collide to create chemical antiphase boundaries, decorated with Fe contact layers and relict disordered layers in a complex landscape. (c) Continuing coarsening of large regions at expense of small regions, with Fe enrichment of small regions.

(5) A key microstructure produced by elimination of all disordered material, except at domain boundaries, consists of large A-ordered regions containing small Fe-enriched B-ordered domains, large B-ordered regions containing small Fe-enriched A-ordered domains with antiphase domain boundaries. An exception is where small Fe-enriched A- and B-ordered domains lie on the edges of the larger regions. Here small Fe-enriched A-ordered domains can be in contact with the large A-ordered regions and small Fe-enriched B-ordered domains may be in contact with larger B-ordered regions where the two phases have the same ordering scheme but different composition. These are 'synphase' boundaries, as distinct from antiphase boundaries. Their magnetic significance will be shown in Paper III.

(6) A T–composition phase diagram in the composition range $X = 0.40$–0.80 was evaluated using schematic G surfaces as a function of $X\mathrm{FeTiO_3}$ and the Fe–Ti order parameter Q. This shows that metastable chemical phase separation can occur during quench related to the disorder to order transition across a wide range of compositions at T's above the tricritical point marking the onset of equilibrium chemical phase separation. The former explains the microtextures and chemical features observed in samples quenched from high T whereas the latter is involved to a limited extent in textural and chemical evolution during subsequent annealing.

(7) Chemical evolution involving the Fe–Ti disorder to order transition from initiation of ordered phases during quench through eventual elimination of the disordered phase and subsequent coarsening with Fe enrichment of smaller ordered regions, provides the necessary microstructures to explain magnetic phenomena at much lower T where chemical reactions are finished. Paper III shows how these properties lead to self-reversed thermoremanent magnetization and room-T magnetic exchange bias.

ACKNOWLEDGMENTS

The research related to this series was supported by grant 189721 from the Research Council of Norway (Nanomat Program) in the EU Matera Program, and visiting fellowships to the Institute of Rock Magnetism, which is supported by an NSF Instruments and Facilities Grant. Significant manuscript preparation took place while Robinson and McEnroe were resident at BGI, Bayreuth, where McEnroe held an EU Marie Curie IE Fellowship in cooperation with Professor Falko Langenhorst. Earlier experimental work at BGI was supported by an EU Access to Infrastructures Grant. The manuscript was improved by comments and suggestions from two perceptive anonymous reviewers; one detected an error in curvature of a spinodal line. To each of these persons and institutions we extend our grateful acknowledgment.

REFERENCES

Allen, S.M. & Cahn, J.W., 1976a. Mechanisms of phase transformations within the miscibility gap of Fe-rich Fe-Al alloys, *Acta Metall.,* **24,** 425–437.

Allen, S.M. & Cahn, J.W., 1976b. On tricritical points resulting from the intersection of lines of higher-order transitions with spinodals, *Scr. Metall.,* **10,** 451–454.

Bosenick, A. *et al*., 2001. Computational methods for the study of energies of cation distributions: applications to cation-ordering phase transitions and solid solutions, *Mineral. Mag.,* **65,** 193–219.

Burton, B.P., 1982. Thermodynamic analysis of the systems $CaCO_3$-$MgCO_3$, α-Fe_2O_3 and Fe_2O_3-$FeTiO_3$, *PhD thesis*, State University of New York at Stony Brook, Stony Brook, NY, pp. 117–118.

Burton, B.P., 1985. Theoretical analysis of chemical and magnetic ordering in the system Fe_2O_3-$FeTiO_3$, *Am. Mineral.,* **72,** 329–336.

Burton, B.P., 1991. The interplay of chemical and magnetic ordering, in *Oxide Minerals: Petrologic and Magnetic Significance*, Reviews in Mineralogy Vol. 25, pp. 301–321, ed. Lindsley, D.H., Min. Soc. America, Washington, DC.

Burton, B.P. & Davidson, P.M., 1988. Multicritical phase relations in minerals, in *Structural and Magnetic Phase Transitions in Minerals,* pp. 60–90, eds Ghose, S., Coey, J.M.D. & Salje, E., Springer-Verlag, New York, NY.

Burton, B.P., Robinson, P., McEnroe, S.A., Fabian, K. & Boffa Ballaran, T., 2008. A low-temperature phase diagram for ilmenite-rich compositions in the system Fe_2O_3-$FeTiO_3$, *Am. Mineral.,* **93,** 1260–1272.

Fabian, K., McEnroe, S.A., Robinson, P. & Shcherbakov, V.P., 2008. Exchange bias identifies lamellar magnetism as the origin of the natural remanent magnetization in titanohematite from ilmenite exsolution, Modum, Norway, *Earth planet. Sci. Lett.,* **268,** 339–353.

Fabian, K., Miyajima, N., Robinson, P., McEnroe, S.A., Boffa Ballaran, T. & Burton, B.P., 2011. Chemical and magnetic properties of rapidly cooled metastable ferri-ilmenite solid solutions—I. Fe-Ti order transition in quenched synthetic Ilm 60, *Geophys. J. Int.,* **186,** 997–1014 (Paper I).

Ghiorso, M.S. & Evans, B.W., 2008. Thermodynamics of rhombohedral oxide solid solutions and a revision of the Fe-Ti two-oxide geothermometer and oxygenbarometer, *Am. J. Sci.,* **308,** 957–1039.

Harrison, R.J., 2006. Microstructure and magnetism in the ilmenite-hematite solid solution: a Monte Carlo simulation study, *Am. Mineral.,* **91,** 1006–1023.

Harrison, R.J. & Becker, U., 2001. Magnetic ordering in solid solutions, *Eur. Mineral. Union Notes Min.,* **3,** 349–383.

Harrison, R.J. & Redfern, S.A.T., 2001. Short- and long-range ordering in the ilmenite-hematite solid solution, *Phys. Chem. Miner.,* **28,** 399–412.

Harrison, R.J., Redfern, S.A.T. & Smith, R.I., 2000. In situ study of the R3- to R3-c phase transition in the ilmenite-hematite solid solution, *Am. Mineral.,* **85,** 1694–1705.

Harrison, R.J., Kasama, T., White, T.A., Simpson, E.T. & Dunin-Borkowski, R.E., 2005. Origin of self-reversed thermoremanent magnetization, *Phys. Rev. Lett.,* **95,** 268501, doi:10.1103/PhysRevLett.95.268501.

Harrison, R.J., McEnroe, S.A., Robinson, P., Carter-Stiglitz, B., Palin, E.J. & Kasama, T., 2007. Low-temperature exchange coupling between Fe_2O_3 and $FeTiO_3$: insight into the mechanism of giant exchange bias in a natural nanoscale intergrowth, *Phys.Rev. B,* **76,** 174436.

Harrison, R.H., McEnroe, S.A., Robinson, P. & Howard, C., 2010. Spin orientation in a natural Ti-bearing hematite: evidence for an out-of plane component, *Am. Mineral.*, **95,** 974–979.

Ishikawa, Y. & Syono, Y., 1963. Order-disorder transformation and reverse thermo-remanent magnetism in the $FeTiO_3$-Fe_2O_3 series, *J. Phys. Chem. Solids,* **24,** 517–528.

Lagroix, F., Banerjee, S.K. & Moskowitz, B.M., 2004. Revisiting the mechanism of reversed thermoremanent magnetization (rTRM) based on observations from synthetic ferrian ilmenite (y = 0.7), *J. geophys. Res.,* **109,** B12108, doi:10.1029/2004JB003076.

McCammon, C., McEnroe, S.A., Robinson P. & Burton, B. P. 2009. Mössbauer spectroscopy used to quantify natural lamellar remanent magnetization in single-grains of ilmeno-hematite, *Earth planet. Sci. Lett.,* **288,** 268–278.

McEnroe, S.A., Carter-Stiglitz, B., Harrison, R.J., Robinson, P., Fabian, K. & McCammon, C., 2007a. Magnetic exchange bias of more than 1 Tesla in a natural mineral intergrowth, *Nat. Nanotechnol.,* **2,** 631–634.

McEnroe, S.A., Robinson, P., Langenhorst, F., Frandsen, C., Terry, M.P. & T. Boffa Ballaran, T., 2007b. Magnetization of exsolution intergrowths of hematite and ilmenite: mineral chemistry, phase relations, and magnetic properties of hemo-ilmenite ores with micron- to nanometer-scale lamellae from Allard Lake, Quebec, *J. geophys. Res.,* **112,** B10103, doi:10.1029/2007JB004973.

Nord, G.L., Jr., 1994. Transformation-induced twin boundaries in minerals, *Phase Transit.,* **48,** 107–134.

Nord, G.L., Jr. & Lawson, C.A., 1989. Order-disorder transition-induced twin domains and magnetic properties in ilmenite-hematite, *Am. Mineral.,* **74,** 160–176.

Nord, G.L., Jr. & Lawson, C.A., 1992. Magnetic properties of ilmenite70 – hematite30: effect of transformation-induced twin boundaries, *J. geophys. Res.,* **97,** 10897–10910.

Pentcheva, R. & Nabi, H., 2008. Interface magnetism in Fe_2O_3/FeTiO3 heterostructures, *Phys. Rev. B*, **77,** doi:10.1103/PhysRevB.77.172405.

Prevot, M., Hoffman, K.A., Goguitchaichvili, A., Doukhan, J-C., Shcherbakov, V. & Bina, M., 2001. The mechanism of self-reversal of thermoremanence in natural hemoilmenite crystals: new experimental data and model, *Phys. Earth planet. Inter.,* **126,** 75–92.

Putnis, A., 1992. *Introduction to Mineral Sciences,* Cambridge University Press, Cambridge, 460pp.

Robinson, P., Harrison, R.J., McEnroe, S.A. & Hargraves, R., 2002. Lamellar magnetism in the hematite-ilmenite series as an explanation for strong remanent magnetization, *Nature,* **418,** 517–520.

Robinson, P., Harrison, R.J., McEnroe, S.A. & Hargraves, R., 2004. Nature and origin of lamellar magnetism in the hematite-ilmenite series, *Am. Mineral.,* 725–747.

Robinson, P., Harrison, R.J. & McEnroe, S.A., 2006. Fe2+ / Fe3+ charge ordering in contact layers of lamellar magnetism: bond valence arguments, *Am. Mineral.,* **91,** 67–72.

Uyeda, S., 1958. Thermo-remanent magnetization as a medium of paleomagnetism, with special reference to reverse thermo-remanent magnetism, *Japan. J. Geophys.,* **2,** 1–123.

APPENDIX A: ENERGY DERIVATIONS RELATED TO FIG. 3

The derivation of eq. (2) follows Bosenick *et al*. (2001). Let W_{AA}, W_{BB} and W_{AB} be the energies associated with A–A, B–B and A–B nearest-neighbour pairs, respectively. Let N_{AA}, N_{BB} and N_{AB} be the total number of A–A, B–B and A–B nearest-neighbour pairs in the system, respectively. The total energy is

$$E = N_{AA}W_{AA} + N_{BB}W_{BB} + N_{AB}W_{AB}. \quad \text{(A1)}$$

If the probability of an A atom sitting next to another A atom is P_{AA}, then

$$N_{AA} = 1/2zN\mathrm{x}_A P_{AA}, \quad \text{(A2)}$$

where z is the coordination number of the lattice ($z = 4$ in this case) and $N = N_A + N_B$ is the total number of atoms in the system. The factor of 1/2 is required to avoid counting each bond twice. N_{AB} and N_{BB} can now be written in terms of N_{AA}

$$N_{AB} = zNx_A(1 - P_{AA}) = zNx_A - 2N_{AA} \quad \text{(A3)}$$

$$N_{BB} = 1/2zN - N_{AA} - N_{AB} = 1/2zN(1 - 2x_A) + N_{AA}. \quad \text{(A4)}$$

Combining eqs (A1), (A3) and (A4), the energy can now be written in terms of N_{AA}

$$E = N_{AA}W_{AA} + [1/2zN(1 - 2x_A) + N_{AA}]W_{BB} + (zNx_A - 2N_{AA})W_{AB} \quad \text{(A4)}$$

$$E = N_{AA}(W_{AA} + W_{BB} - 2W_{AB}) + 1/2zN[(1 - 2x_A)W_{BB} + 2x_A W_{AB}] \quad \text{(A4)}$$

$$E = E_0 - JN_{AA}, \quad \text{(A5)}$$

where $J = (2W_{AB} - W_{AA} - W_{BB})$ and $E_0 = 1/2zN[(1–2x_A)W_{BB} + 2x_A W_{AB}]$. E_0 is constant for a given composition and can be discarded during the simulations. A positive value of J means that A–A bonds are energetically favourable and the system will attempt to maximize the number of A–A nearest-neighbour pairs. A negative value of J means that A–A bonds are energetically unfavourable. The system will attempt to avoid A–A nearest-neighbour pairs.

During a Monte Carlo simulation, two atoms are chosen at random and their positions are swapped. The change in energy of the system (ΔE) is calculated by counting the change in the number of A–A bonds before and after the swap and multiplying by J. If ΔE is negative then the swap is accepted. If ΔE is positive, then the swap is accepted with a probability $\exp(-\Delta E/RT)$, where R is the gas constant, T is temperature. The process is then repeated many thousands of times, until the system approaches equilibrium. The simulations in Fig. 3 were performed with $J = -5000$, $T = 10$ and 1×10^6 steps.

APPENDIX B: IONIC CHARGE BALANCE OF OXYGEN BETWEEN CATION LAYERS: THE CONTACT LAYER ARGUMENT

Table B1 illustrates three models for (001) interfaces between ordered and anti-ordered phases of composition $X = 0.60$. A Q value of 0.733 has been chosen for the ordered phase that gives relatively simple layer compositions.

Model L shows the situation where ordered Ti layers are juxtaposed against ordered Ti layers or where ordered Fe^{2+} layers are juxtaposed against ordered Fe^{2+} layers. Here, the overcharge on oxygens along the common interface of two Ti-rich layers is very large (+2.292) and undercharge on oxygens along common interface of two Fe^{2+}-rich layers is also very large (+1.708). This is a highly unstable situation.

Model M shows the situation where ordered Ti and Fe layers are separated by single disordered layers. Undercharge on oxygens along common interfaces between ilmenite Fe^{2+} layers and disordered layers is now +1.854 greater than undercharge of 1.708 in Model L. Overcharge on oxygens along common interface of ilmenite–Ti layers and disordered layers is now +2.146, less than overcharge of 2.292 in Model L. These values are still far from +2.0 and hence probably are also not stable.

Table B1. General charge balance.

Model L ordered ilmenite 60 ($Q = 0.733$) without contact layers

1 # # # # # # #	*Ilmenite Ti*	$Ti^{4+}_{0.52}\ Fe^{2+}_{0.08}\ Fe^{3+}_{0.4}$	*Mean chg. 3.44+*	*Mean B.S. 0.573*
*2 * * * * * * ***	*Ilmenite Fe*	$Ti^{4+}_{0.08}\ Fe^{2+}_{0.52}\ Fe^{3+}_{0.4}$	*Mean chg. 2.56+*	*Mean B.S. 0.427*
3 # # # # # # #	*Ilmenite Ti*	$Ti^{4+}_{0.52}\ Fe^{2+}_{0.08}\ Fe^{3+}_{0.4}$	*Mean chg. 3.44+*	*Mean B.S. 0.573*
*4 * * * * * * ***	*Ilmenite Fe*	$Ti^{4+}_{0.08}\ Fe^{2+}_{0.52}\ Fe^{3+}_{0.4}$	*Mean chg. 2.56+*	*Mean B.S. 0.427*
5 # # # # # # #	*Ilmenite Ti*	$Ti^{4+}_{0.52}\ Fe^{2+}_{0.08}\ Fe^{3+}_{0.4}$	*Mean chg. 3.44+*	*Mean B.S. 0.573*
*6 * * * * * * ***	*Ilmenite Fe*	$Ti^{4+}_{0.08}\ Fe^{2+}_{0.52}\ Fe^{3+}_{0.4}$	*Mean chg. 2.56+*	*Mean B.S. 0.427*
7 # # # # # # #	*Ilmenite Ti*	$Ti^{4+}_{0.52}\ Fe^{2+}_{0.08}\ Fe^{3+}_{0.4}$	*Mean chg. 3.44+*	*Mean B.S. 0.573*
8 # # # # # # #	**Ilmenite Ti**	$\mathbf{Ti^{4+}_{0.52}\ Fe^{2+}_{0.08}\ Fe^{3+}_{0.4}}$	**Mean chg. 3.44+**	**Mean B.S. 0.573**
9 * * * * * * *	**Ilmenite Fe**	$\mathbf{Ti^{4+}_{0.08}\ Fe^{2+}_{0.52}\ Fe^{3+}_{0.4}}$	**Mean chg. 2.56+**	**Mean B.S. 0.427**
10 # # # # # #	**Ilmenite Ti**	$\mathbf{Ti^{4+}_{0.52}\ Fe^{2+}_{0.08}\ Fe^{3+}_{0.4}}$	**Mean chg. 3.44+**	**Mean B.S. 0.573**
11 * * * * * *	**Ilmenite Fe**	$\mathbf{Ti^{4+}_{0.08}\ Fe^{2+}_{0.52}\ Fe^{3+}_{0.4}}$	**Mean chg. 2.56+**	**Mean B.S. 0.427**
12 # # # # # #	**Ilmenite Ti**	$\mathbf{Ti^{4+}_{0.52}\ Fe^{2+}_{0.08}\ Fe^{3+}_{0.4}}$	**Mean chg. 3.44+**	**Mean B.S. 0.573**
13 * * * * * *	**Ilmenite Fe**	$\mathbf{Ti^{4+}_{0.08}\ Fe^{2+}_{0.52}\ Fe^{3+}_{0.4}}$	**Mean chg. 2.56+**	**Mean B.S. 0.427**
*14 * * * * * ***	*Ilmenite Fe*	$Ti^{4+}_{0.08}\ Fe^{2+}_{0.52}\ Fe^{3+}_{0.4}$	*Mean chg. 2.56+*	*Mean B.S. 0.427*
15 # # # # # #	*Ilmenite Ti*	$Ti^{4+}_{0.52}\ Fe^{2+}_{0.08}\ Fe^{3+}_{0.4}$	*Mean chg. 3.44+*	*Mean B.S. 0.573*
*16 * * * * * ***	*Ilmenite Fe*	$Ti^{4+}_{0.08}\ Fe^{2+}_{0.52}\ Fe^{3+}_{0.4}$	*Mean chg. 2.56+*	*Mean B.S. 0.427*
17 # # # # # #	*Ilmenite Ti*	$Ti^{4+}_{0.52}\ Fe^{2+}_{0.08}\ Fe^{3+}_{0.4}$	*Mean chg. 3.44+*	*Mean B.S. 0.573*
*18 * * * * * ***	*Ilmenite Fe*	$Ti^{4+}_{0.08}\ Fe^{2+}_{0.52}\ Fe^{3+}_{0.4}$	*Mean chg. 2.56+*	*Mean B.S. 0.427*
19 # # # # # #	*Ilmenite Ti*	$Ti^{4+}_{0.52}\ Fe^{2+}_{0.08}\ Fe^{3+}_{0.4}$	*Mean chg. 3.44+*	*Mean B.S. 0.573*
*20 * * * * * ***	*Ilmenite Fe*	$Ti^{4+}_{0.08}\ Fe^{2+}_{0.52}\ Fe^{3+}_{0.4}$	*Mean chg. 2.56+*	*Mean B.S. 0.427*

Mean oxygen charge balance in different locations (without bond valence)

Between *ilmenite Ti layer 7* and **ilmenite Ti layer 8**

Two cations, mean B.S. = 0.573; two cations, mean B.S. = 0.573. Charge on oxygen +2.292 (big overcharge)

Between **ilmenite Fe layer 13** and *ilmenite Fe layer 14*

Two cations, mean B.S. = 0.427, two cations, mean B.S. = 0.427. Charge on oxygen +1.708 (big undercharge)

Model M ordered ilmenite 60 ($Q = 0.733$) separated by disordered layers

1 # # # # # # #	*Ilmenite Ti*	$Ti^{4+}_{0.52}\ Fe^{2+}_{0.08}\ Fe^{3+}_{0.4}$	*Mean chg. 3.44+*	*Mean B.S. 0.573*
*2 * * * * * * ***	*Ilmenite Fe*	$Ti^{4+}_{0.08}\ Fe^{2+}_{0.52}\ Fe^{3+}_{0.4}$	*Mean chg. 2.56+*	*Mean B.S. 0.427*
3 # # # # # # #	*Ilmenite Ti*	$Ti^{4+}_{0.52}\ Fe^{2+}_{0.08}\ Fe^{3+}_{0.4}$	*Mean chg. 3.44+*	*Mean B.S. 0.573*
*4 * * * * * * ***	*Ilmenite Fe*	$Ti^{4+}_{0.08}\ Fe^{2+}_{0.52}\ Fe^{3+}_{0.4}$	*Mean chg. 2.56+*	*Mean B.S. 0.427*
5 # # # # # # #	*Ilmenite Ti*	$Ti^{4+}_{0.52}\ Fe^{2+}_{0.08}\ Fe^{3+}_{0.4}$	*Mean chg. 3.44+*	*Mean B.S. 0.573*
*6 * * * * * * ***	*Ilmenite Fe*	$Ti^{4+}_{0.08}\ Fe^{2+}_{0.52}\ Fe^{3+}_{0.4}$	*Mean chg. 2.56+*	*Mean B.S. 0.427*
7 D D D D D	Disordered	$Ti^{4+}_{0.3}\ Fe^{2+}_{0.3}\ Fe^{3+}_{0.4}$	Mean chg. 3+	Mean B.S. 0.5
8 # # # # # # #	**Ilmenite Ti**	$\mathbf{Ti^{4+}_{0.52}}\ Fe^{2+}_{0.08}\ \mathbf{Fe^{3+}_{0.4}}$	**Mean chg. 3.44+**	**Mean B.S. 0.573**
9 * * * * * * *	**Ilmenite Fe**	$\mathbf{Ti^{4+}_{0.08}\ Fe^{2+}_{0.52}\ Fe^{3+}_{0.4}}$	**Mean chg. 2.56+**	**Mean B.S. 0.427**
10 # # # # # #	**Ilmenite Ti**	$\mathbf{Ti^{4+}_{0.52}\ Fe^{2+}_{0.08}\ Fe^{3+}_{0.4}}$	**Mean chg. 3.44+**	**Mean B.S. 0.573**
11 * * * * * *	**Ilmenite Fe**	$\mathbf{Ti^{4+}_{0.08}\ Fe^{2+}_{0.52}\ Fe^{3+}_{0.4}}$	**Mean chg. 2.56+**	**Mean B.S. 0.427**
12 # # # # # #	**Ilmenite Ti**	$\mathbf{Ti^{4+}_{0.52}\ Fe^{2+}_{0.08}\ Fe^{3+}_{0.4}}$	**Mean chg. 3.44+**	**Mean B.S. 0.573**
13 * * * * * *	**Ilmenite Fe**	$\mathbf{Ti^{4+}_{0.08}\ Fe^{2+}_{0.52}\ Fe^{3+}_{0.4}}$	**Mean chg. 2.56+**	**Mean B.S. 0.427**
14 D D D D D	Disordered	$Ti^{4+}_{0.3}\ Fe^{2+}_{0.3}\ Fe^{3+}_{0.4}$	Mean chg. 3+	Mean B.S. 0.5
15 # # # # # #	*Ilmenite Ti*	$Ti^{4+}_{0.52}\ Fe^{2+}_{0.08}\ Fe^{3+}_{0.4}$	*Mean chg. 3.44+*	*Mean B.S. 0.573*
*16 * * * * * ***	*Ilmenite Fe*	$Ti^{4+}_{0.08}\ Fe^{2+}_{0.52}\ Fe^{3+}_{0.4}$	*Mean chg. 2.56+*	*Mean B.S. 0.427*
17 # # # # # #	*Ilmenite Ti*	$Ti^{4+}_{0.52}\ Fe^{2+}_{0.08}\ Fe^{3+}_{0.4}$	*Mean chg. 3.44+*	*Mean B.S. 0.573*
*18 * * * * * ***	*Ilmenite Fe*	$Ti^{4+}_{0.08}\ Fe^{2+}_{0.52}\ Fe^{3+}_{0.4}$	*Mean chg. 2.56+*	*Mean B.S. 0.427*
19 # # # # # #	*Ilmenite Ti*	$Ti^{4+}_{0.52}\ Fe^{2+}_{0.08}\ Fe^{3+}_{0.4}$	*Mean chg. 3.44+*	*Mean B.S. 0.573*
*20 * * * * * ***	*Ilmenite Fe*	$Ti^{4+}_{0.08}\ Fe^{2+}_{0.52}\ Fe^{3+}_{0.4}$	*Mean chg. 2.56+*	*Mean B.S. 0.427*

Mean oxygen charge balance in different locations

Between *ilmenite Fe layer 6* and disordered layer 7

Two cations, mean B.S. = 0.427; two cations, mean B.S. = 0.5. Charge on oxygen +1.854 (undercharge)

Between disordered layer 7 and **ilmenite Ti layer 8**

Two cations w mean B.S. = 0.5, two cations, mean B.S. = 0.573. Charge on oxygen +2.146 (overcharge)

Between **ilmenite Fe layer 13** and disordered layer 14

Two cations, mean B.S. = 0.427; two cations, mean B.S. = 0. 5. Charge on oxygen +1.854 (undercharge)

Between disordered layer 14 and *ilmenite Ti layer 15*

Two cations w mean B.S. = 0.5, two cations, mean B.S. = 0.573. Charge on oxygen +2.146 (overcharge)

Table B1. (*Continued.*)

Model N ordered ilmenite 60 ($Q = 0.733$) separated by two contact layers and two disordered layers

1 # # # # # # #	*Ilmenite Ti*	*$Ti^{4+}_{0.52}$ $Fe^{2+}_{0.08}$ $Fe^{3+}_{0.4}$*	*Mean chg. 3.44+*	*Mean B.S. 0.573*
*2 * * * * * * ***	*Ilmenite Fe*	*$Ti^{4+}_{0.08}$ $Fe^{2+}_{0.52}$ $Fe^{3+}_{0.4}$*	*Mean chg. 2.56+*	*Mean B.S. 0.427*
3 # # # # # # #	*Ilmenite Ti*	*$Ti^{4+}_{0.52}$ $Fe^{2+}_{0.08}$ $Fe^{3+}_{0.4}$*	*Mean chg. 3.44+*	*Mean B.S. 0.573*
4 C C C C C	Contact Fe	$Ti^{4+}_{0.19}$ $Fe^{2+}_{0.41}$ $Fe^{3+}_{0.4}$	Mean chg. 2.78+	Mean B.S. 0.463
5 D D D D D	Disorder	$Ti^{4+}_{0.3}$ $Fe^{2+}_{0.3}$ $Fe^{3+}_{0.4}$	Mean chg. 3+	Mean B.S. 0.5
6 D D D D D	Disorder	$Ti^{4+}_{0.3}$ $Fe^{2+}_{0.3}$ $Fe^{3+}_{0.4}$	Mean chg. 3+	Mean B.S. 0.5
7 C C C C C	Contact Fe	$Ti^{4+}_{0.19}$ $Fe^{2+}_{0.41}$ $Fe^{3+}_{0.4}$	Mean chg. 2.78+	Mean B.S. 0.463
8 # # # # # # #	**Ilmenite Ti**	**$Ti^{4+}_{0.52}$ $Fe^{2+}_{0.08}$ $Fe^{3+}_{0.4}$**	**Mean chg. 3.44+**	**Mean B.S. 0.573**
9 * * * * * * *	**Ilmenite Fe**	**$Ti^{4+}_{0.08}$ $Fe^{2+}_{0.52}$ $Fe^{3+}_{0.4}$**	**Mean chg. 2.56+**	**Mean B.S. 0.427**
10 # # # # # # #	**Ilmenite Ti**	**$Ti^{4+}_{0.52}$ $Fe^{2+}_{0.08}$ $Fe^{3+}_{0.4}$**	**Mean chg. 3.44+**	**Mean B.S. 0.573**
11 * * * * * * *	**Ilmenite Fe**	**$Ti^{4+}_{0.08}$ $Fe^{2+}_{0.52}$ $Fe^{3+}_{0.4}$**	**Mean chg. 2.56+**	**Mean B.S. 0.427**
12 # # # # # # #	**Ilmenite Ti**	**$Ti^{4+}_{0.52}$ $Fe^{2+}_{0.08}$ $Fe^{3+}_{0.4}$**	**Mean chg. 3.44+**	**Mean B.S. 0.573**
13 C C C C C	Contact Fe	$Ti^{4+}_{0.19}$ $Fe^{2+}_{0.41}$ $Fe^{3+}_{0.4}$	Mean chg. 2.78+	Mean B.S. 0.463
14 D D D D D	Disorder	$Ti^{4+}_{0.3}$ $Fe^{2+}_{0.3}$ $Fe^{3+}_{0.4}$	Mean chg. 3+	Mean B.S. 0.5
15 D D D D D	Disorder	$Ti^{4+}_{0.3}$ $Fe^{2+}_{0.3}$ $Fe^{3+}_{0.4}$	Mean chg. 3+	Mean B.S. 0.5
16 C C C C C	Contact Fe	$Ti^{4+}_{0.19}$ $Fe^{2+}_{0.41}$ $Fe^{3+}_{0.4}$	Mean chg. 2.78+	Mean B.S. 0.463
17 # # # # # # #	*Ilmenite Ti*	*$Ti^{4+}_{0.52}$ $Fe^{2+}_{0.08}$ $Fe^{3+}_{0.4}$*	*Mean chg. 3.44+*	*Mean B.S. 0.573*
*18 * * * * * * ***	*Ilmenite Fe*	*$Ti^{4+}_{0.08}$ $Fe^{2+}_{0.52}$ $Fe^{3+}_{0.4}$*	*Mean chg. 2.56+*	*Mean B.S. 0.427*
19 # # # # # # #	*Ilmenite Ti*	*$Ti^{4+}_{0.52}$ $Fe^{2+}_{0.08}$ $Fe^{3+}_{0.4}$*	*Mean chg. 3.44+*	*Mean B.S. 0.573*
*20 * * * * * * ***	*Ilmenite Fe*	*$Ti^{4+}_{0.08}$ $Fe^{2+}_{0.52}$ $Fe^{3+}_{0.4}$*	*Mean chg. 2.56+*	*Mean B.S. 0.427*

Mean oxygen charge balance in different locations

Between *ilmenite Ti layer 3* and Fe contact layer 4

Two cations, mean B.S. = 0.573; two cations, mean B.S. = 0.463. Charge on oxygen +2.072 (overcharge)

Between Fe contact layer 4 and disordered layer 5

Two cations w mean B.S. = 0.463, two cations, mean B.S. = 0.5. Charge on oxygen +1.926 (undercharge)

Between disordered layer 6 and Fe contact layer 7

Two cations w mean B.S. = 0.5, two cations, mean B.S. = 0.463. Charge on oxygen +1.926 (undercharge)

Between Fe contact layer 7 and **ilmenite Ti layer 8**

Two cations, mean B.S. = 0.463; two cations, mean B.S. = 0.573. Charge on oxygen +2.072 (overcharge)

Between **ilmenite Ti layer 12** and Fe contact layer 13

Two cations, mean B.S. = 0.573; two cations, mean B.S. = 0.463. Charge on oxygen +2.072 (overcharge)

Between Fe contact layer 13 and disordered layer 14

Two cations w mean B.S. = 0.463, two cations, mean B.S. = 0.5. Charge on oxygen +1.926 (undercharge)

Between disordered layer 15 and Fe contact layer 16

Two cations w mean B.S. = 0.5, two cations, mean B.S. = 0.463. Charge on oxygen +1.926 (undercharge)

Between Fe contact layer 16 and *ilmenite Ti layer 17*:

Two cations, mean B.S. = 0.463; two cations, mean B.S. = 0.573. Charge on oxygen +2.072 (overcharge)

Model N shows the situation where pairs of ordered Ti layers are separated by two Fe contact layers and two disordered layers. The use of intervening Fe contact layers creates a greater opportunity for charge imbalance reduction than use of disordered layers only. By this means, undercharges are reduced to +1.926 and overcharges to +2.072, which is the best that has been achieved with standard lamellar magnetism without use of bond-valence calculations as shown in Table B2. However the Fe contact layers also introduce an important new requirement. The two contact layers on the contacts of the ordered regions must be separated by two disordered layers. Thus, the two disordered layers can be considered as a residual of the original disordered host before ordering, and can't be diminished further.

In summary, the process of producing domains of ordered and anti-ordered solid solution during cooling necessarily involves impingement of ordered regions onto disordered regions and gradual merging of ordered and anti-ordered regions. Charge balance considerations indicate that the disordered remainders should not become thinner than two cation layers across (001). Furthermore, charge balance considerations also strongly favour Fe contact layers one cation thick along (001) boundaries between disordered and ordered phases. This would suggest that the minimum thickness of (001) interfaces between two ordered phases would consist of two disordered layers and two contact layers.

Unlike the case of high-T ilmenite–haematite intergrowths, magnetic interactions play no role in the chemical ordering process. However, strong chemical interactions dictate that hypothetical Ti-rich contact layers that are realistic from charge balance considerations only, are unrealistic in terms of other chemical interactions. For this reason only Fe-rich contact layers that are a chemical average between disordered 'haematite layers' and Fe-rich ilmenite ordered layers are used. It is envisioned that as the ordering process proceeds across a disordered region, Fe-rich contact layers will occur along all (001) interfaces as they travel across the bulk material. Likely the same scenario will be involved as very thin interfaces between ordered regions travel across the bulk material during coarsening, but charge balance suggests that such interfaces will likely consist of at least two disordered 'haematite' layers and two contact layers throughout the movements. The charge imbalance created at these interfaces, even when ameliorated by contact layers, is one of several reasons why these interfaces are eliminated by coarsening over remarkably short times.

Table B2. Charge balance including bond valence.

The bond-valence approach to contact layers was outlined by Robinson *et al*. 2006. In this, bond strength is tied to bond length by a formula involving a constant for each ion. In most of the calculations here it has been necessary to make the compromise of using mean atoms. In the rhombohedral oxide structure there are long and short cation–oxygen bonds within the octahedrons, so amongst Fe^{3+}, Fe^{2+} and Ti^{4+} there are the following six bond strengths.

Fe^{3+} Short	0.604	Fe^{3+} Long	0.381
Fe^{2+} Short	0.372	Fe^{2+} Long	0.268
Ti^{4+} Short	0.852	Ti^{4+} Long	0.479

Following is a bond strength argument for an Fe contact layer between pure haematite above and a pure ilmenite Ti layer below, as given in Robinson *et al*. 2006, table 4(a). We also show a parallel argument for a Ti contact layer between pure haematite above and a pure ilmenite Fe layer below. Although the second model succeeds for charge balance, the Ti contact layer is considered improbable on the basis of chemical interaction parameters and not considered further.

Charge order model B Fe contact layer		**Charge order model A Ti contact layer**	
Top of contact layer		Top of contact layer	
Short Fe3+	0.604	Short Fe3+	0.604
Long Fe3+	0.381	Long Fe3+	0.381
Long Fe2+	0.268	Long Ti4+	0.479
Short Fe3+	0.604	Short Fe3+	0.604
Total charge	**1.857**	Total Charge	**2.068**
Bottom of contact layer		Bottom of contact layer	
Short Fe2+	0.372	Short Ti4+	0.852
Long Fe3+	0.381	Long Fe3+	0.381
Long Ti4+	0.479	Long Fe2+	0.268
Short Ti4+	0.852	Short Fe2+	0.372
Total charge	**2.084**	Total charge	**1.873**

Before considering contact layers in Ilm 60 intergrowths, we consider briefly charge balance within disordered and ordered $X = 0.60$. For the ordered layers we use the compositions for $Q = 0.733$ in Table B1. In these calculations mean atoms must be used.

Disordered Fe^{3+}0.4, Fe^{2+}0.3, Ti^{4+}0.3 **Disordered Fe^{3+}0.4, Fe^{2+}0.3, Ti^{4+}0.3**			
Position	Fraction	B.S.	Contribution
(1) Short Fe3+	0.4	0.604	0.2416
Short Fe2+	0.3	0.372	0.1116
Short Ti4+	0.3	0.852	0.2556
(2) Long Fe3+	0.4	0.381	0.1524
Long Fe2+	0.3	0.268	0.0804
Long Ti4+	0.3	0.479	0.1437
(3) Long Fe3+	0.4	0.381	0.1524
Long Fe2+	0.3	0.268	0.0804
Long Ti4+	0.3	0.479	0.1437
(4) Short Fe3+	0.4	0.604	0.2416
Short Fe2+	0.3	0.372	0.1116
Short Ti4+	0.3	0.852	0.2556
Total charge			**1.9706**

Ordered Fe layer Fe^{3+}0.4, Fe^{2+}0.52, Ti^{4+}0.08 **Ordered Ti layer Fe^{3+}0.4, Fe^{2+}0.08, Ti^{4+}0.52**			
Position	Fraction	B.S.	Contribution
(1) Short Fe3+	0.4	0.604	0.2416
Short Fe2+	0.52	0.372	0.1934
Short Ti4+	0.08	0.852	0.0682
(2)Long Fe3+	0.4	0.381	0.1524
Long Fe2+	0.52	0.268	0.1394
Long Ti4+	0.08	0.479	0.0383
(3)Long Fe3+	0.4	0.381	0.1524
Long Fe2+	0.08	0.268	0.0214
Long Ti4+	0.52	0.479	0.2491
(4) Short Fe3+	0.4	0.604	0.2416
Short Fe2+	0.08	0.372	0.0216
Short Ti4+	0.52	0.852	0.4430
Total charge			**1.9706**

In the disordered and ordered single phases, calculated charge balance is the same at 1.9706. The very slight difference from 2, merely reflects minor imperfections in the bond-valence system.

APPENDIX C: SHORT-RANGE CATION MOVEMENT DURING Fe–Ti ORDERING

The simplicity of cation movement needed to produce ordered from disordered phases in composition $X = 0.60$ is illustrated in Fig. C1. This makes use of the rules for Fe contact layers detailed in Appendix B; to portray compositions in terms of single atoms it is necessary to multiply the Fe contact layer composition $Fe^{3+}{}_{0.40}$, $Fe^{2+}{}_{0.45}$, $Ti^{4+}{}_{0.15}$ by 20, thus giving a layer composition with integral numbers of ions, $Fe^{3+}{}_{8}$, $Fe^{2+}{}_{9}$, $Ti^{4+}{}_{3}$. Because formally, at least, there is no change in position of Fe^{3+} ions, they can be ignored and we then become concerned only with exchanges of Fe^{2+} and Ti^{4+} ions within a total of 12 positions in each layer. In this portrayal, a disordered layer contains 6 Ti ions (black in Fig. C1) and 6 Fe^{2+} ions (white in Fig. C1), a Ti ordered layer contains 12 Ti ions, an Fe ordered layer contains 12 Fe^{2+} ions and an Fe contact layer contains 3 Ti ions and 9 Fe^{2+} ions as in the formula above. The four parts of Fig. C1 show four steps in the growth of an ordered lamella in a disordered host.

In the first step (Fig. C1a, reaction 1), which initiates the growth of an ordered lamella, six Ti ions from two disordered layers are

Table B2. (*Continued.*)

Next we compare imbalance where a single disordered layer is placed against a Ti ordered layer or an Fe ordered layer, and where a single Fe contact layer is placed between a disordered layer and a Ti ordered layer.

No contact layer
Disordered Fe^{3+}0.4, Fe^{2+}0.3, Ti^{4+}0.3
Ordered Ti layer Fe^{3+}0.4, Fe2 + 0.08 Ti^{4+}0.52
Relative to one oxygen

Position	Fraction	B.S.	Contribution
(1)Short Fe3+	0.4	0.604	0.2416
Short Fe2+	0.3	0.372	0.1116
Short Ti4+	0.3	0.852	0.2556
(2) Long Fe3+	0.4	0.381	0.1524
Long Fe2+	0.3	0.268	0.0804
Long Ti4+	0.3	0.479	0.1437
(3) Long Fe3+	0.4	0.381	0.1524
Long Fe2+	0.08	0.268	0.0214
Long Ti4+	0.52	0.479	0.2491
(4) Short Fe3+	0.4	0.604	0.2416
Short Fe2+	0.08	0.372	0.0298
Short Ti4+	0.52	0.852	0.4430
Total charge			**2.1226**

Disordered Fe^{3+}0.4, Fe^{2+}0.3, Ti^{4+}0.3
Fe contact layer Fe^{3+}0.4, Fe^{2+}0.45, Ti^{4+}0.15
Ordered Ti layer Fe^{3+}0.4, Ti^{4+}0.6
Top of contact layer

Position	Fraction	B.S.	Contribution
(1) Short Fe3+	0.4	0.604	0.2416
Short Fe2+	0.3	0.372	0.1116
Short Ti4+	0.3	0.852	0.2556
(2)Long Fe3+	0.4	0.381	0.1524
Long Fe2+	0.3	0.268	0.0804
Long Ti4+	0.3	0.479	0.1437
(3)Long Fe3+	0.4	0.381	0.1524
Long Fe2+	0.41	0.268	0.1099
Long Ti4+	0.19	0.479	0.0910
(4) Short Fe3+	0.4	0.604	0.2416
Short Fe2+	0.41	0.372	0.1525
Short Ti4+	0.19	0.852	0.1619
Total charge			**1.8946**

Disordered Fe^{3+}0.4, Fe^{2+}0.3, Ti^{4+}0.3
Ordered Fe Layer Fe^{3+}0.4, Fe^{2+}0.52, Ti4 + 0.08
Relative to one oxygen

Position	Fraction	B.S.	Contribution
(1)Short Fe3+	0.4	0.604	0.2416
Short Fe2+	0.3	0.372	0.1116
Short Ti4+	0.3	0.852	0.2556
(2) Long Fe3+	0.4	0.381	0.1524
Long Fe2+	0.3	0.268	0.0804
Long Ti4+	0.3	0.479	0.1437
(3) Long Fe3+	0.4	0.381	0.1524
Long Fe2+	0.52	0.268	0.1394
Long Ti4+	0.08	0.479	0.0383
(4) Short Fe3+	0.4	0.604	0.2416
Short Fe2+	0.52	0.372	0.1934
Short Ti4+	0.08	0.852	0.0682
Total charge			**1.8186**

Bottom of contact layer

Position	Fraction	B.S.	Contribution
(5) Short Fe3+	0.4	0.604	0.2416
Short Fe2+	0.41	0.372	0.1525
Short Ti4+	0.19	0.852	0.1619
(6)Long Fe3+	0.4	0.381	0.1524
Long Fe2+	0.41	0.268	0.1099
Long Ti4+	0.19	0.479	0.0910
(7)Long Fe3+	0.4	0.381	0.1524
Long Fe2+	0.08	0.268	0.0214
Long Ti4+	0.52	0.479	0.2416
(8) Short Fe3+	0.4	0.604	0.2416
Short Fe2+	0.08	0.372	0.0298
Short Ti4+	0.52	0.852	0.4430
Total charge			**2.0466**

When a disordered layer is juxtaposed against a Ti ordered layer (left above) there is an overcharge of 2.1226. When a disordered layer is juxtaposed against an Fe ordered layer (left below) there is an undercharge of 1.8186. When an Fe contact layer is placed between a disordered layer above and a Ti ordered layer below (right), there is a small undercharge of 1.8946 on the top of the contact layer and a small overcharge of 2.0466 on the bottom of the contact layer. This combination provides the greatest reduction in charge imbalance. The fact that the undercharge is more below 2 than the overcharge is above 2 only reflects minor imperfections in the bond-valence method. The two numbers average 1.9706.

moved to form a single Ti ordered layer, with Fe^{2+} ions moving in the opposite direction. The two disordered layers then become Fe contact layers. This can be recognized as the first step in lamellar growth in Fig. 5. All subsequent steps (Fig. C1b–d, reaction 2) involve changes only on one side of the lamella, but still involve one-layer jumps between three layers. Here six Ti ions are moved to form a single Ti ordered layer from a disordered layer. Three of the Ti ions come from an Fe contact layer, changing it into an Fe ordered layer. Three others come from a disordered layer turning it into an Fe contact layer. Reaction 2 is repeated twice to produce an ordered lamella consisting of three Ti ordered layers, two Fe ordered layers and two contact layers (see Robinson *et al*. 2004).

Every step involves the movement of six Ti ions into a Ti ordered layer from two adjacent layers and the movement of six Fe^{2+} ions out of that layer and into the two adjacent layers. There are no steps where jumps of ions of more than one layer are required. This, in part, may explain why Fe–Ti ordering can occur during rapid cooling, in contrast to the process of exsolution of near-end-member haematite and ilmenite where long-distance diffusion of ions is needed.

APPENDIX D: EXPLANATION OF SPINODAL BOUNDARIES EXTENDING FROM THE TRICRITICAL POINT

The use of Gibbs free energy versus composition diagrams to explain binary phase relations is covered in many textbooks (*cf*. Putnis 1992), not least the special phenomena involving metastable

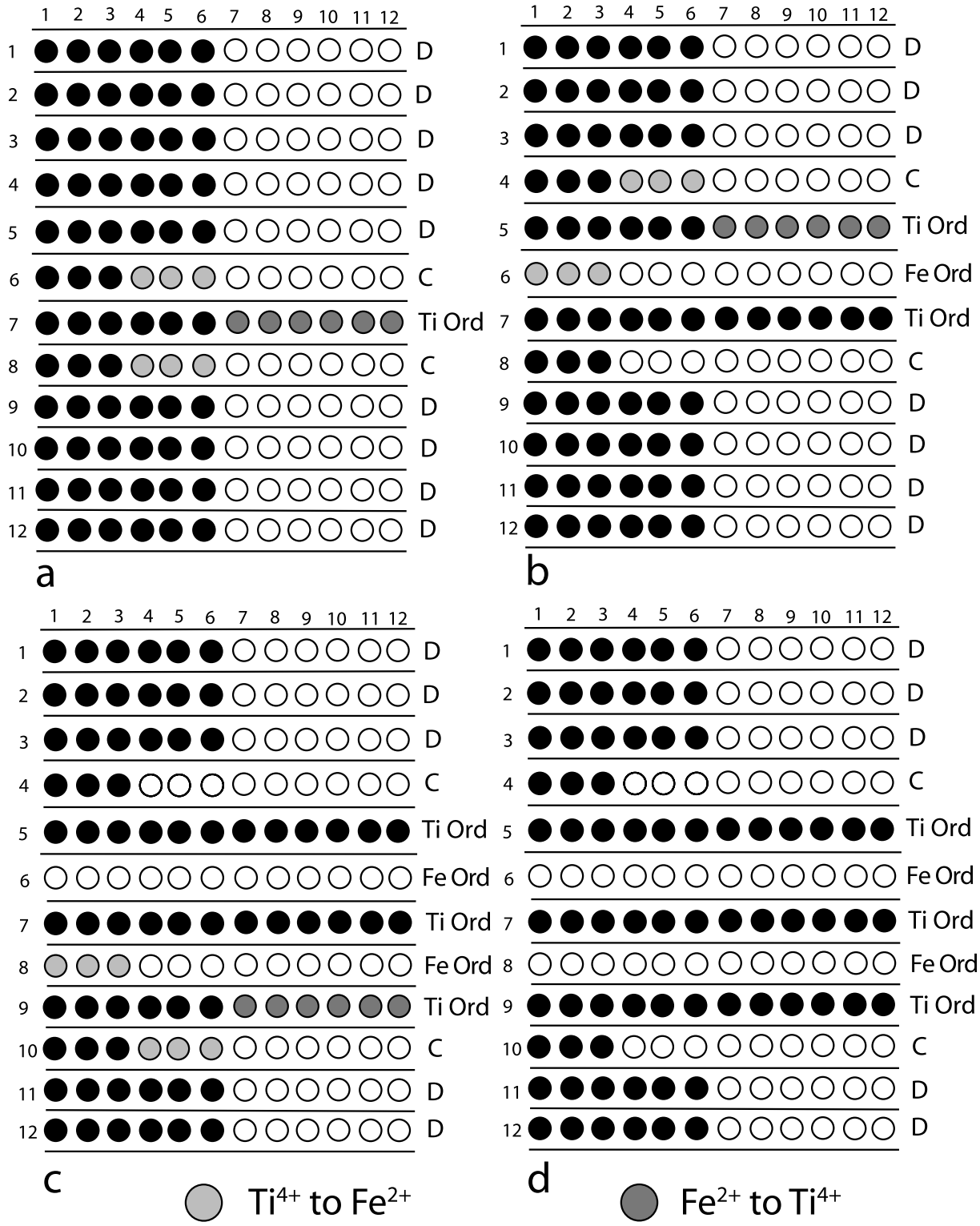

Figure C1. Simple illustration of atomic moves required to grow a lamella of ordered composition $X = 0.60$ from a disordered solid solution of the same composition. (a) Initiation of ordered lamella from disordered phase by reaction 1. Six Ti ions move from two disordered layers into Ti ordered layer. Three Fe^{2+} ions move in opposite direction creating two Fe contact layers. (b) Growth on top of lamella by reaction 2. Three Ti ions move from Fe contact layer up to new Ti ordered layer, and three Fe^{2+} ions move opposite way creating the first Fe ordered layer. Above this three Ti ions move from disordered layer to Ti ordered layer and three Fe^{2+} ions move opposite way creating new Fe contact layer. (c) Growth on bottom of lamella again by reaction 2. (d) Final product after three growth steps – an ordered lamella with three Ti ordered layers, two Fe ordered layers, and two Fe contact layers.

spinodal curves related to a binary miscibility gap. A tutorial on this subject cannot be given here. However, the detailed relationships surrounding a binary tricritical point are sufficiently challenging and sufficiently easy to forget, that we provide an example.

Allen and Cahn (1976a, b) presented a set of G versus composition diagrams for the vicinity of a tricritical point that illustrate the spinodal effects (Fig. 10) and are almost exactly applicable to the phase diagram of Harrison (2006) as in Fig. 8(a). Two curves of G versus composition are used, one for the disordered phase and one for the ordered. At high-T both curves are convex down and they are tangent to each other at a point on both curves representing the disorder–order transition. The curve for the disordered phase extends over a broad composition range, both to higher and lower compositions (in our case XIlm) than the disorder–order point. By contrast the curve for the ordered phase begins exactly at the disorder–order point and extends away from it only in one direction, in our case towards higher XIlm. This means that towards lower XIlm there is only the disordered curve whereas towards higher XIlm the ordered curve has a lower G, but the disordered curve also exists metastably with a higher G.

Equilibrium chemical phase separation begins at highest T at the tricritical point. This is the exact position where a small downward 'bump' appears on the G curve for the ordered phase and begins to move towards higher XIlm from the tricritical point. Establishment of the bump immediately establishes two additional features. (1) A tangent line from the bump on the ordered curve inevitably is also tangent to a part of the disordered curve that lies at lower XIlm than the disorder–order intersection point. This means that at any T below the tricritical point, the disorder to order transition is metastable with respect to the two-phase mixture. This is a salient feature shown in all the versions of the haematite–ilmenite phase diagram. (2) Establishment of the bump also immediately creates a convex upward part of the ordered curve and an inflection point on the ordered curve at lower XIlm than the tangent point in (1) above. This is a spinode and the region between this spinode and the disorder–order point becomes the region where chemical spinodal decomposition can take place. The name 'tricritical point' appears to be named by the fact that this point is where three points coincide. It is also the vanishing point where there had been two inflection points on the ordered curve as well as the point of the disorder–order transition on both curves.